Sensitivity analysis of hybrid methods for the flow around the ahmed body with application to passive control with rounded edges

Francois Delassaux, Iraj Mortazavi, Emmanuelle Itam, Vincent Herbert, Charles Ribes

Sensitivity analysis of hybrid methods for the flow around the Ahmed body with application to passive control with rounded edges

Francois Delassaux, Iraj Mortazavi, Emmanuelle Itam, Vincent Herbert & Charles Ribes

Abstract A comparative study of SST RANS and three hybrid approaches (SAS, DDES and SBES methods) is performed to analyse the flow around the 25° Ahmed body. The DDES approach is then selected as the reference model, based on comparison of numerical results. The main study is based on grid and time step influence over the simulation results. All results are compared to in-house experiments. The three grids $15l$, $20l$ and $30l$ (related to the number of prism layers in the boundary layer) show a fair prediction for both drag C_d and lift C_l coefficients. The best prediction is obtained with the $30l$ grid with an accurate prediction of C_d and C_l values as well as the main flow characteristics, compared to experiments. Another part of this paper focuses on the time step effect on the computational accuracy. Then, the flow around various rounded edge Ahmed body configurations is compared to experiments in order to validate the robustness of the numerical methodology. The rounded edge flow topologies are therefore deeply investigated. It is shown that they act as passive flow control and significantly influence the flow topology and aerodynamical coefficients. In fact, the rounded strategy modifies the flow detachment and weakens the onset of C-pillar vortices, which directly reduce drag and lift coefficients.

Key words: turbulence modeling, hybrid methods, Ahmed body, rounded and sharp edges, passive flow control.

Francois Delassaux - Emmanuelle Itam - Iraj Mortazavi
Equipe M2N, CNAM Paris, 292 rue Saint-Martin, 75003 Paris, FRANCE
e-mail: francois.delassaux@ext.mpsa.com

Vincent Herbert - Charles Ribes
Groupe PSA, Route de Gisy, 78943 Velizy-Villacoublay, FRANCE

Nomenclature

α	Radii of rounded edge over the backlight of the Ahmed body
β	Radii of rounded edge over the side of the Ahmed body
Δx^+	Dimensionless cell distance in streamwise direction
Δy^+	Dimensionless cell distance in spanwise direction
Δz^+	Dimensionless wall distance in vertical direction
δ	Boundary layer thickness
Δ_{max}	Maximum local grid spacing in the 3 directions
ν	Kinematic viscosity
ν_t	Turbulent viscosity
ν_t/ν	Turbulent viscosity ratio
ω	Specific turbulence dissipation rate
φ	angle between horizontal line and the rear slanted surface
BCD	Bounded Central Differencing scheme
C_d	Drag coefficient
C_l	Lift coefficient
C_p	Pressure coefficient
C_{DES}	Constant of DDES model
$CAFE$	Corporate Average Fuel Economy
CD	Central Differencing scheme
Cd_1	Coefficient of DDES model
CFD	Computational Fluid Dynamics
CFL	Courant Friedrichs Levy number
$DDES$	Delayed Detached Eddy Simulation
DNS	Direct Numerical Simulation
f_d	Shielding function of DDES model
f_{SBES}	Shielding function of SBES model
G	Ahmed body ground clearance

GIS	Grid Induced Separation
H_B	Ahmed body height
I	Turbulent intensity
k_m	Modeled turbulent kinetic energy
k_r	Resolved turbulent kinetic energy
k_t	Total turbulent kinetic energy
L	Length of the horizontal projection of the rear slanted surface
L_B	Ahmed body length
L_R	Length of the recirculation bubble over the rear slanted surface
L_t	Length scale of the modeled turbulence in SAS model
L_{ref}	Edge length of a regular tetrahedron
L_{VB}	Length of the recirculation bubble behind the vertical base
L_{vk}	Von Kármán length scale in SAS model
LES	Large Eddy Simulation
MSD	Modeled Stress Depletion
Q	Q criterion - second invariant of the velocity gradient
Q_{SAS}	Additional source term in the ω equation for SAS model
r	Ratio between Δ_{max} over δ for DDES model
R_0S_0	Ahmed body with sharp edges
R_0S_{10}	Ahmed body with rounded edges on the sides
$R_{10}S_0$	Ahmed body with rounded edges on the roof
$R_{10}S_{10}$	Ahmed body with double rounded edges on the roof and sides
$RANS$	Reynolds-Averaged Navier-Stokes
Re_H	Reynolds number based on the height of the body
Rer	Rounded edge over the backlight of the Ahmed body
Res	Rounded edge over the side of the Ahmed body
S	Strain rate magnitude
S_t	Strouhal number
SAS	Scale-Adaptive Simulation
$SBES$	Stress-Blended Eddy Simulation
SF	Stretch Factor
SRS	Scale Resolving Simulation
SST	Shear Stress Transport
$U^{'}$	First derivative of velocity
$U^{''}$	Second derivative of velocity

V_∞ Freestream velocity

W_B Ahmed body width

X^* Dimensionless X length by L

Y^* Dimensionless Y length by L

Z^* Dimensionless Z length by L

1 Introduction

The automotive industry is facing drastic restrictions regarding greenhouse gas emissions, with the European "CAFE 2020" objective of mean global CO_2 emission of 95 g/km for every car manufacturer. To achieve this goal, several components of vehicle must be improved: engine must be greener (now considering electric engines), global mass reduced and aerodynamic performances improved. Reducing greenhouse gas emissions and fuel consumption from aerodynamic drag is one of the main issues for engineers. Bluff body flows are characterized by regions of separated flows containing wide spectra of turbulent scales. These regions are mainly responsible for drag and lift forces applied on the body. Turbulence modeling must be capable of giving a fair prediction of separation to accurately capture the global flow features as well as drag and lift coefficients, crucial for automotive industry engineers. Hence, the purpose of this work is to fine-tune a robust Scale Resolving Simulations (SRS) procedure on 25° Ahmed bodies flow before moving on to real vehicles.

The Ahmed body [1] is a generic simplified car which reproduces many of flow features visible on a real vehicle, such as the 3D recirculation in the wake of the body and the longitudinal vortices. The longitudinal vortices are found around the front window edges (A-pillar vortices) and at the back of notchback shape vehicle (C-pillar vortices) for instance. The most challenging case for computational simulation around Ahmed body is the one with a rear slant angle of 25°. The 25° Ahmed body is a very complex case with strong longitudinal vortices, a closed recirculation bubble on the rear slanted surface and 3D wake structure. In fact, as Ahmed et al. [1] showed, the longitudinal vortices are generated for slant angles between 12.5° and 30°. For higher angles, the flow becomes massively separated, reaching a quasi two-dimensional behavior for the square back geometry [7]. For these reasons, the 25° Ahmed body is a very interesting benchmark to validate different simulations approaches, that will be used later on real car geometries.

Steady state or transient Reynolds Averaged Navier-Stokes (RANS) simulations, commonly used in the car industry, fail to correctly predict the flow around 25° Ahmed body ([14], [18]). Direct Numerical Simulations (DNS) are very accurate but drastically expensive ([8], [9]) even for lower Reynolds number flow.

On the other hand, Large Eddy Simulation (LES) has shown interesting numerical achievements ([26], [35] and [36]). Krajnović and Davidson [26] reduced the freestream velocity from 40 m/s, corresponding to a Reynolds number based on the height of the body of $Re_H = 7.68 \times 10^5$, in classical studies to 10.4 m/s with $Re_H = 2 \times 10^5$, in order to

decrease the high numerical cost of LES simulations. The authors argued that the reduced velocity has no influence over the flow topology which is lead by the geometric separation at the back of the body. Consequently, the finer grid selected was made of 16 million cells, making LES resolution affordable. This study meticulously detailed the flow topology, especially the onset of the longitudinal vortices. The low influence over the flow topology of the Reynolds number decrease is confirmed in the work of Minguez et al. [36] where the authors studied the same flow with a very low Reynolds number, $Re_H = 8322$ and the classical one $Re_H = 7.68 \times 10^5$. They showed that the flow topology is almost similar between the two Reynolds numbers. The only change is the longer recirculation areas (at the forehand and the rear slanted surfaces) for the lower Reynolds number due to lower velocity around the body. Moreover, Minguez et al. [35] and [36] used a Spectral Vanishing Viscosity (SVV) LES technique with volume penalization method to study this flow. The authors showed that the separation at the front of the body directly influences the separation at the back. The separation is delayed compared to experiments, leading to poor prediction of turbulent kinetic energy profiles in the separation area. On the second half of the rear slanted surface, SVV-LES model correctly predicts the turbulent kinetic energy level. However, the prohibitive numerical cost of LES for industrial flows under high Reynolds numbers makes it impossible to use for a real car geometry in a close future.

Hence, an SRS approach is needed to represent the wide scales and spectra of turbulence for such case. A few studies showed Detached Eddy Simulations (DES) and Delayed Detached Eddy Simulation (DDES) capabilities for the flow prediction around Ahmed body. The DES97 approach [47] was used by Kapadia et al. [25] using Spalart-Allmaras (SA) underlying RANS model. The authors faced Modeled-Stress Depletion (MSD) because of LES intrusion in the boundary layer, as the mesh is not fine enough to handle LES resolution in the boundary layer. As a consequence, the flow separates massively on the rear slant surface. Menter and Kuntz [33] observed a fully stalled flow on the rear window with Shear Stress Transport (SST) RANS model. Using SST DES, a closed recirculation bubble was observed, even though the time-averaged solution did not closely match with experiments. The coarse grid used in this study could explain the results discrepancy from experiments. Guilmineau et al. [15] used SST DES with different shielding functions, defined as $F_{DES} = 0$, F_1 and F_2 in order to switch from RANS to LES resolutions, with F_1 and F_2 the functions of SST RANS model. Both the shielding functions $F_{DES} = 0$ and F_1 captures the separation/attachment phenomenon on the rear slant surface, even though the recirculation bubble length was overestimated. Because of the construction of the F_2 function, which over-protects the boundary layer, the SST-F_2 DES predicted a massive separation flow, similar to a classical SST RANS model. Guilmineau et al. [17] showed some improvements in flow prediction around the Ahmed body using Improved Delayed DES model (IDDES) [46]. However, as the IDDES model is very sensitive to empirical tuning in the wall region, its superiority over DDES model depends on studied case [43]. Consequently, its robustness can be questionable for its use on real vehicle shapes. Finally, Ashton and Revell [3] demonstrated the accuracy of the DDES model using both SST and $\phi - f$ underlying RANS models. An Embedded DDES (E-DDES) approach was also developed. Globally, the E-DDES approach is superior to the DDES, based on flow topology observations in the symmetry plane. However, the model adaptation to a more complex geometry seems more difficult.

Most of the literature is focused on numerical and experimental studies of the sharp edges Ahmed body. At this stage, passive flow control study is rather limited on this case and mostly from experiments point of view. As the rear slant surface and the vertical base represent around 70% of the total drag of the Ahmed body, an investigation must be carried out on this part in order to reduce the drag force, with the final aim to replicate this on a real vehicle. Thacker et al. [50] developed a rounded edge at the transition between the roof and the rear slant surface with a 40% radius of curvature of the projected length of the rear window ($201mm$). The authors showed that the recirculation bubble on the rear window vanishes and leads to a drag reduction of 10% and lift decrease around 1.5%. Moreover, the suppression of the separation directly influences the shape of the 3D wake behind the vertical base of the body, leading to a longer 3D recirculation which tends also to locally reduce drag. More recently, Rossitto et al. [41] extends the rounded edges concepts with three new Ahmed bodies: a roof rounded case, a side rounded case and a double rounded case combining both roof and side rounded edges. First, the author showed that a radius of curvature of 10% is enough to suppress the separation on the rear slant surface with the roof rounded case, leading to a drag decrease of 16% and lift increase of 7%. In this configuration, the C-pillar vortices are quite identical in strength compared to the sharp case. As a consequence, the evolution of aerodynamic coefficients is mainly due to the lack of separation on the rear slant surface and the longer 3D wake behind the body. For the second case with rounded edges on the side of the body, the author found a drag increase of 3% and lift decrease of 22%. In this case, the recirculation length is increased from 78% for the sharp case to 85% for the side rounded edges case, leading to quite constant drag on the rear window from the recirculation.

However, to our knowledge, there is no computational study on the rounded edge configurations. The above mentioned experimental observations need to be enriched by numerical simulations. The physical behavior is tremendously different from sharp to rounded. A comprehensive analysis of the flow dynamics is necessary to achieve a better understanding of drag and lift forces evolution. In this work, numerical simulations are performed to investigate the flow behaviors for all rounded edge geometries. Here, the sides of the body are rounded and the onset of the longitudinal vortices is delayed and intensity inside the core of the vortices highly reduced, leading to huge lift reduction. The flow topology on this case highlights two key points: the strength of the C-pillar vortices influences the recirculation length (lower intensity leads to longer recirculation) and the shape of the wake behind the vertical base. Indeed, the core of the two counter-rotating recirculation zones is closer to the vertical surface, leading to a local drag increase, which compensates the drag reduction of the C-pillar over the rear window. By combining both roof and side rounded edges, the double rounded case shows a drag and lift reduction of respectively 16% and 18% linked to the flow topology features described above.

In the first part of this paper, a comparative study is performed on SST RANS, SAS, DDES and SBES turbulence models for the flow around the 25° Ahmed body with the target of fine-tuned a robust and accurate computational methodology. Then, the DDES approach is chosen as the reference method. After an exhaustive numerical grid convergence study, this technique is used to study and analyze in details the flow around the 25° Ahmed bodies with sharp

and rounded edges. As described above, the main purpose of this work is to study the effects of various rounded edges features on the flow topology and aerodynamic performances. Because the major role on the drag force of the rear window recirculation bubble, the rounded edges are concentrated around this part of the geometry. Three cases are studied: the roof rounded edges, the side rounded edges and the double rounded edges. Based on the numerical methodology developed on the sharp edges case, the authors will investigate passive flow control on rounded Ahmed bodies using CFD methods and define the best location for rounded edges on the back of the body.

All numerical results are compared to in-house experiments (pressure coefficients C_p, velocity and turbulent kinetic energy profiles, longitudinal vortices etc.) ([23] and [40]) in order to verify the accuracy and robustness of the numerical method. The main characteristics of these complex flows are then studied.

The paper is organized as follows: Sect. 2 describes the sharp and rounded edges Ahmed body geometries used in the numerical study and the global flow topologies. Sect. 3 details the turbulence modeling approaches. Then, Sect. 4 gives details on the three grids considered and the numerical setup used. Sect. 5 is dedicated to the sharp edges Ahmed body and highlights the performances of RANS, SAS, DDES and SBES turbulence modeling techniques focusing on the numerical convergence of the selected method and compares results between CFD and experiments. Sect. 6 deals with passive flow control with rounded edges around the back of the Ahmed body. For each of rounded edges configurations, the accuracy is validated compared to experiments and then the flow behavior is studied and compared between sharp and rounded edges geometries in order to characterize the best passive control strategy.

2 Sharp and rounded edges Ahmed bodies

In this part, the classical 25° Ahmed body with sharp edges and Ahmed bodies with rounded edges are presented regarding geometries and flow behavior. The aim of this part is to set the context of the following study. The numerical procedure is developed on the sharp case as it is the most famous benchmark for automotive industry. Many turbulent and numerical parameters have been carefully studied: the turbulence method, grid refinement, numerical schemes and time step influence. Moreover, the main study is based on averaged flow field compared to in-house experiments carried out by Rossitto [40]. In addition, we have studied unsteady flow behavior. This global study around the sharp edges case ensure the robustness of our numerical methodology, before moving on the rounded edges cases.

2.1 Ahmed body with sharp edges

The Ahmed body [1] is a simplified real car, made of a forebody, a long mid-section assumed to suppress interactions between the front and the back of the body and a variable rear slant angle. The rear slant surface and the vertical base are called afterbody. The surface under the body is called underbody. The length, width, and height of the body are

respectively $L_B = 1044$ mm, $W_B = 380$ mm and $H_B = 288$ mm. The angle φ between horizontal line and the rear slant surface is equal to 25°. The body is fixed to the wind tunnel ground with four feet of 30 mm diameter and a ground clearance of $G = 50$ mm. The origin of the (x,y,z) axis is located at the vertical base of the body, on the ground, see Fig. 1. Besides, the length of the horizontal projection of the rear slant surface is defined as $L = 201$ mm and used for normalize X, Y and Z locations denoted with starred values as X^*, Y^* and Z^*. The transition roof/rear slanted surface and the end of the rear window respectively corresponds to $X^* = -1$ and $X^* = 0$. The symmetry plane is denoted $Y^* = 0$ and two offset planes are defined as $Y^* = 0.5$ and $Y^* = 0.9$. The maximum of Y^* is equal to 0.97. Velocity, vorticity and turbulent kinetic energy are respectively made dimensionless using V_∞, L/V_∞ and V_∞^2, with V_∞ defined as the freestream velocity.

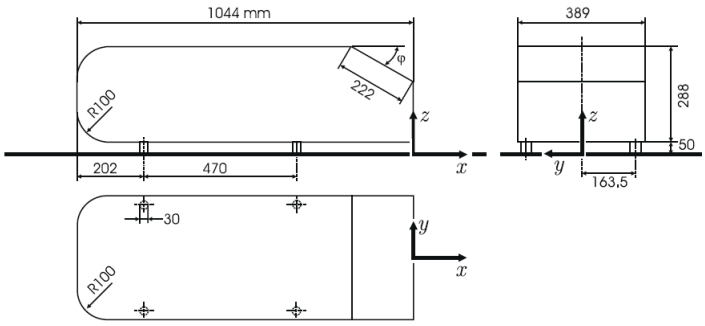

Fig. 1 25°Ahmed body geometry

The mean flow topology around the Ahmed body is shown in Fig. 2. This flow representation is provided by Ahmed et al. experimental work [1]. For the reader transparency, the flow around the Ahmed body is decomposed in two parts: the one around the rear slant surface and the one around the vertical base called 'wake' in this study. The sharp transition between the roof and the rear slanted surface lead to a closed separation bubble. The sharp edges on the sides of the Ahmed body's back is responsible for the onset of a pair of counter-rotating longitudinal vortices, the so-called C-pillar vortex. The wake is characterized by two recirculation areas behind the vertical base: one coming from the slanted surface and the other from the underbody. Though the flow topology is well know by the scientific community, there is no consensus over the length of the recirculation bubble over the slanted surface. Many lengths are reported in the literature from 50% to almost 100% for similar Reynolds number. The length of the closed separation bubble is strongly influenced by the experimental geometry (sharpness of the transition roof/slanted surface) setup, as well as the wind tunnel used.

Our numerical results are compared to Rossitto's experiments [40], carried out in La Ferté Vidame (France) Groupe PSA's wind tunnel. This Eiffel wind tunnel has a blockage ratio of 1.4 %. The Ahmed body was placed on an elevated surface. A 6 component balance was used to measure the aerodynamic forces. The errors of the measurements precision for drag and lift coefficients are respectively $\pm 0.5\%$ and $\pm 1.0\%$ of the measured quantities. The body was equipped by 115 probes over the rear to evaluate the static pressure coefficient C_p. 2D and 3D Particle Image Velocimetry (PIV)

measurements were used to visualize the flow in iso Y planes: the symmetry plane and an offset plane, respectively called $Y^* = 0$ and $Y^* = 0.5$. Moreover, the evolution of the longitudinal vortices was studied by Jermann [23] on the same body in the same wind tunnel. More details is given in [40]. In this paper, drag and lift coefficients (respectively denoted C_d and C_l) as well as velocity and turbulent kinetic energy profiles and C_p are validated with the above mentioned experiments.

In this work, we will mainly focus on the prediction of drag and lift coefficients which are crucial for fuel consumption and vehicle stability in automotive industry and the flow topology around the back of the body (the closed recirculation bubble and the C-pillar vortices).

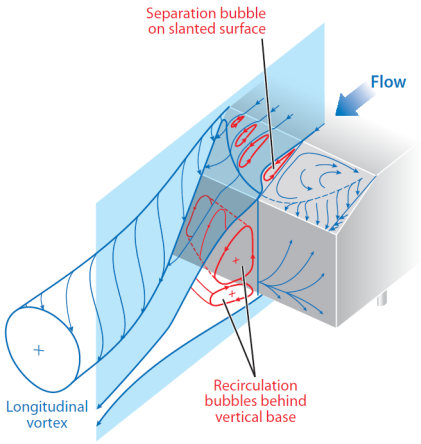

Fig. 2 Global flow topology around 25° Ahmed body - from Choi [11]

2.2 Ahmed body with rounded edges

The flow separation on the back (rear window and sides) of the sharp edges Ahmed body generates a closed recirculation bubble and high energetic C-pillar vortices with a high drag contribution. Some simple geometrical modifications can improve the flow behavior and alter the recirculation bubble and the C-pillar vortices. Rounded edges can introduce a passive control strategy with beneficial effect on the drag and lift forces.

Based on the work detailed previously, the numerical procedure has been validated on new Ahmed bodies with rounded edges. These bodies were studied experimentally by Rossitto et al. [41] and described hereafter. In this section, the modifications in the flow topology due to the influence of the rounded edges is investigated compared to the reference case with sharp edges. Drag and lift coefficients and flow evolutions are compared on the $20l$ and $30l$ grids, for a CFL number around 3.

The shape and the locations of the rounded edges are reported in Fig. 3 in blue color. *Rer* stands for the upper edge of the backlight, at the roof junction and *Res* for the sides edges. The geometries are then noted $R_\alpha S_\beta$, where R stands for $Roof$ and S for $Side$. α and β represent the values of the radii. The radius of curvature of rounded edges is equal to

10% of the reference length $L = 201$ mm, i.e 20.1 mm. The reference Ahmed body with sharp edges is referred as R_0S_0.

Based on these two locations of rounded edges, we can generate three different Ahmed bodies, respectively called:

- side rounded, R_0S_{10}, reducing the C-pillar vortices intensity
- roof rounded, $R_{10}S_0$, suppressing the bubble separation
- double rounded, $R_{10}S_{10}$, combining both side and roof rounded effects

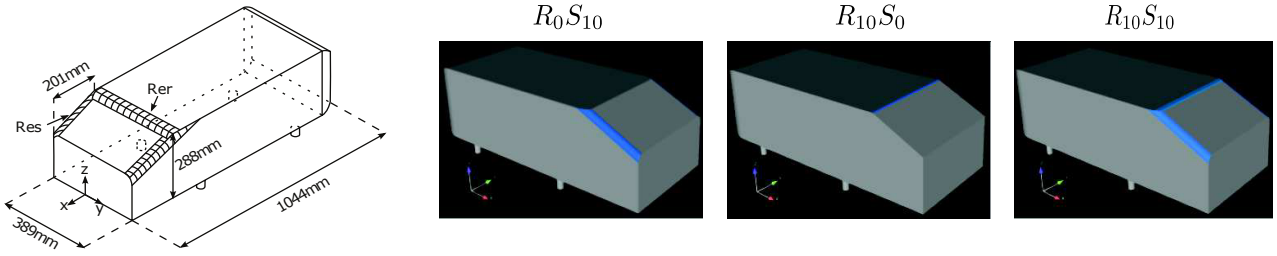

Fig. 3 Schematic representation of the Ahmed body with rounded edges at the back from [41], R_0S_{10}, $R_{10}S_0$ and $R_{10}S_{10}$

3 Turbulence modeling approaches

3.1 Numerical methods discussion

The choice of the numerical method is crucial in order to obtain the best accuracy possible from computations. Three main categories of numerical approaches are traditionally considered: Direct Numerical Simulations (DNS), Large Eddy Simulations (LES) and Reynolds-Averaged Navier-Stokes (RANS). Due to the direct representation and computation of the Navier-Stokes equations, i.e resolving the entire spectrum of the energy, DNS approach requires huge grid refinement and very small time step for flows with high Reynolds number, as considered around a real car and an airfoil for instance. Consequently, this approach is not practicable for now. The RANS approach, based on the averaged of the Navier-Stokes equations, relies on a full modeling of the flow, i.e modeling the entire spectrum of the energy. This approach is widely used in the engineering community, due to the numerical robustness and the very low computational time required with such model. For example, the flow around a full scale vehicle can be studied in four hours on 120 cores using RANS model. However, due to the modeling aspect of this model, mean flows can be rather wrong compared to experiments. The third approach, the LES one, is situated between RANS and DNS resolution, regarding flow resolution and consequently numerical cost. A large part of the energy spectrum is resolved, while the scales smaller compared to the grid size (generally identified as the dissipation range in the turbulent spectrum) are modeled using Sub-grid scale models. However, the LES approach requires a very fine grid in the boundary layer, which is currently not achievable for a turbulent flow around a full scale car. More recently, hybrid RANS/LES approaches were developed to take advantages from both RANS and LES formulations. RANS is then used in the boundary layer where

LES requires non affordable grid. When separation is detected, the model switches to LES mode in order to resolve as much scales as possible, based on grid refinement. To confirm these statements, different numerical approaches are used in this work. The first one is the Shear Stress Transport RANS model [31] for fast computations. Then, the Scale Adaptive Simulation (SAS) is used. This model is an improved URANS formulation developed by Menter and Egorov [34] where resolution switch from RANS to LES due to the activation of a source term in the transport equation for the specific turbulence dissipation rate ω. Finally, two hybrid RANS/LES approaches are considered: Delayed Detached Eddy Simulation (DDES) [48] and Stress-Blended Eddy Simulation (SBES) [2]. The main purpose of this work is to determine the best numerical model to analyze and predict the flow around the 25° Ahmed body. The four models studied are then briefly explained in the next sections.

3.2 Turbulence models

3.2.1 SST RANS model

SST RANS model is known as one of the more accurate turbulence model for separation prediction compared to $k-\varepsilon$ and $k-\omega$ formulations. SST model combines the strengths of $k-\omega$ in the boundary layer and gradually switches to a $k-\varepsilon$ formulation in the outer part of the boundary layer to liberate from freestream dependency of the $k-\omega$ model [30]. The blending between $k-\varepsilon$ and $k-\omega$ formulations is ensured with the F1 blending function. This model is sensitized to adverse pressure gradient by taking into account the shear stress transport, modifying the eddy viscosity formulation in the boundary layer of the model, with the blending function F2 (more details on the construction of the model can be found in [31]).

Moreover, this model requires a resolution down to the wall, so that the first node of the mesh must be put in the viscous-sub layer as $y^+ \simeq 1$. This feature of the model is respected in the build process of the grids detailed in Sect. 4.

3.2.2 Scale-Adaptive Simulation - SAS

SAS is an improved URANS formulation developed by Menter and Egorov [34] based on Rotta's work [42]. This approach allows the representation of the large scales of turbulence, which is not the case with traditional $k-\varepsilon$ and $k-\omega$ RANS models. The authors modify and adapt the Rotta's model to the $k-\omega$ SST approach, defining the SST SAS model. The only difference between RANS and SAS formulations is the additional source term denoted Q_{SAS} in the transport equation for the specific turbulence dissipation rate ω:

$$Q_{SAS} = max\left[\rho\eta_2\kappa S^2\left(\frac{L_t}{L_{vk}}\right)^2 - C\cdot\frac{2\rho k}{\sigma_\phi}max\left(\frac{1}{\omega^2}\frac{\partial\omega}{\partial x_j}\frac{\partial\omega}{\partial x_j},\frac{1}{k^2}\frac{\partial k}{\partial x_j}\frac{\partial k}{\partial x_j}\right),0\right] \quad (1)$$

Where ρ, κ, S^2, L_t, L_{vk}, k and ω are respectively the density, the von Kármán constant, the strain rate magnitude, the length scale of the modeled turbulence, the von Kármán length scale, the turbulent kinetic energy and the specific

turbulence dissipation rate. η_2, C and σ_ϕ are constant parameters. The von Kármán length scale is defined as follows:

$$L_{vk} = \kappa \left| \frac{U'}{U''} \right| \tag{2}$$

With $U' = \sqrt{2S_{ij}S_{ij}}$, $U'' = \sqrt{\frac{\partial^2 U_i}{\partial x_k^2}\frac{\partial^2 U_i}{\partial x_j^2}}$ and $S_{ij} = \frac{1}{2}\left(\frac{\partial U_i}{\partial x_j} + \frac{\partial U_j}{\partial x_i}\right)$. The second derivative U'' term detects instabilities in the flow, and then allows the break-up of large unsteady structure into a turbulent spectrum. This is possible by the reduction of the eddy viscosity, allowing flow fluctuations. The source term Q_{SAS} dominates the other terms of the ω equation under unsteady conditions, then activates the full SAS functionality, acting as LES subgrid model. All of the quantities are phase-averaged based on URANS mode construction, as SAS model is a URANS formulation with a source term.

3.2.3 Delayed/Detached Eddy Simulation models - DES/DDES

Spalart et al. [47] proposed a hybrid RANS/LES formulation, the so-called Detached Eddy Simulation or DES97. The main purpose of this model is to use the strong points of both RANS and LES computation in different parts of the flow in order to reduce the computational cost with a little loss of accuracy. The grid refinement is prohibitive in the near wall region (attached boundary layer) for LES computation, so that, in this flow area, DES97 model will act as RANS model. In massively separated regions, RANS models are known to suffer from inaccurate prediction of flow recirculation and recirculation length. As a consequence, in order to resolve as much as possible scales, LES is activated in this flow area. To achieve this blending between RANS and LES formulations, the dissipative term in the k equation of the SST RANS model is modified as follows [51]:

$$Y_k = \rho\beta^* k\omega => Y_k = \rho\beta^* \frac{k^{3/2}}{l_{DES}} \tag{3}$$

with β^* a constant of the SST RANS model and l_{DES} the modified length scale of the DES model defined as

$$l_{DES} = min(l_{RANS}, l_{LES}) \tag{4}$$

$$l_{RANS} = \frac{\sqrt{k}}{\beta^*\omega} \tag{5}$$

$$l_{LES} = C_{DES}\,\Delta_{max} \tag{6}$$

With Δ_{max} the maximum local grid spacing defined as $\Delta_{max} = max(\Delta_x, \Delta_y, \Delta_z)$ and $C_{DES} = C_{DES1}.F_1 + C_{DES2}.(1 - F_1)$ with $C_{DES1} = 0.78$ and $C_{DES2} = 0.61$.

The switch between RANS and LES occurs when $\Delta_{max} < \delta$ with δ the boundary layer thickness. In a boundary layer, Δ_{max} is lead by the streamwise (x) and spanwise (y) resolution of the wall, as the vertical direction (z) is refined a lot compared to the two others directions, so $\Delta_{max} = max(\Delta_x, \Delta_y)$. Violating this criterion can lead to destruction of the numerical simulation. Menter and Kuntz [33] faced Grid-Induced Separation (GIS) due to high grid refinement in the

boundary layer. This phenomenon has been renamed by Spalart et al. [48] as Modeled-Stress Depletion (MSD). MSD happens when LES penetrates the upper part of the boundary layer where the grid is not fine enough to resolve the velocity fluctuations. Then, the model reduced the eddy viscosity, leading to transfer from modeled stress to resolved stress while the grid cannot sustain LES resolution. In this context, GIS happens. In reality, GIS is a consequence of MSD. Moreover, a classical problem appears for all hybrid RANS-LES methods and was identified in the DES97 publication [47]: the grey area. It corresponds to flow area where the transition between RANS and LES is occurring. In this area, the initial lack of resolved turbulence results in neither RANS nor LES resolution.

The reader is referred to Mockett PhD work [37] for more details on DES.

Spalart et al. [48] improved the protection of the boundary layer, yielding to the Delayed DES model (DDES). For DDES model, the shielding function takes into account both the distance to the wall and eddy-viscosity field, which is time-dependent. The delay function f_d is defined as follows by Spalart et al. [48]:

$$f_d = 1 - tanh\left[(Cd_1 r_d)^{Cd_2}\right] \tag{7}$$

The r_d parameter represents the ratio of a model length scale to the wall distance. The f_d function is designed to be equal to 1 in LES region, where $r_d \ll 1$, and 0 elsewhere when $r_d > 1$. The constants Cd_1 and Cd_2 are respectively 20 and 3 to ensure a fair protection of boundary layer with SST model [13]. The DDES length scale reads as follows:

$$l_{DDES} = l_{RANS} - f_d\, max(0, l_{RANS} - l_{LES}) \tag{8}$$

This new formulation of the shielding function ensures a stronger protection of the boundary layer from LES intrusion. Menter [32] defines the ratio $r = \frac{\Delta_{max}}{\delta}$ and shows that the impact of grid refinement is delayed to $r < 0.2$ in DDES, compared to $r < 1$ in DES. It shows the GIS phenomenon is strongly reduced with this new formulation of the model. Moreover, the grey area is reduced due to faster transition from RANS to LES [48].

It can be shown under the assumption of local equilibrium (i.e. equality of the generation and dissipation terms of the transport equations) that DDES sub-grid scale model reduces to Smagorinsky-Lilly model [45].

3.2.4 Stress-Blended Eddy Simulation - SBES

SBES is a new hybrid RANS-LES turbulence model with a modified formulation, compared to DDES, giving the ability to switch from underlying RANS model directly to any existing algebraic LES model [2]. In this study, the LES resolution is made by the Wall-Adapting Local Eddy-viscosity (WALE) model [38]. A new shielding function has been built for the SBES model, called f_{SBES}. This function theoretically enhances the shielding function compared to DDES by a better protection of the RANS wall boundary layer region against influences from the LES mode. This function has not been published yet. The shielding function f_{SBES} achieves the blending on the stress level between RANS and LES formulations as follows:

$$\tau_{ij}^{SBES} = f_{SBES}\tau_{ij}^{RANS} + (1 - f_{SBES})\,\tau_{ij}^{LES} \tag{9}$$

The same formulation is done for the blending of eddy viscosity. Moreover, the transition from RANS to LES is faster compared to DDES in separation area, due to the low stress levels enforced by the LES model. It also reduces significantly the eddy viscosity levels. This new formulation represents a new type of hybrid RANS-LES approach with the ability to choose both RANS and LES models.

4 Computational setup

4.1 Computational domain setup

The computational domain, schematized in Fig. 4, is respectively $5L_B$ long upstream with L_B the length of the Ahmed body, equal to $L_B = 1.044m$ and $10L_B$ long downstream of the Ahmed body. The cross section of domain is equal to $4.2L_B$ and its height is set to $5L_B$. The blockage ratio is computed as the ratio between the frontal area of the body over the inlet section of the numerical wind tunnel. It gives a blockage ratio of $0,5\%$. The inlet boundary condition is defined as velocity inlet with $V_\infty = 40\ m/s$, leading to a Reynolds number based on the height of the body Re_H equal to 7.68×10^5. Turbulent quantities at the inlet are set as: the viscosity ratio ν_t/ν, defined as the ratio of turbulent viscosity ratio ν_t over the kinematic viscosity ν, is equal to 10 and the turbulent intensity I is set to 1.6% as in experiments. A pressure outlet condition is applied to the exit surface, with gauge pressure equal to 0 Pa. No-slip wall boundary conditions have been applied on the body based on the integration of the governing equations down to the wall itself. The same boundary conditions are used on the sides and the roof of the computational domain. The use of no-slip wall condition is possible as the blockage ratio is very low and it has no influence on the global flow. From experiments [40], the boundary layer thickness is equal to 25 mm in the center of the wind tunnel without any body. To reproduce the experimental boundary layer thickness, the ground of the computational domain is divided into two parts: from the inlet to $X/L_B = -3$, a slip wall condition is applied and the remainder part of the ground is defined as a no-slip wall condition to allow the build up of the boundary layer. This is the simplest way to reproduce experimental boundary layer thickness. It is also possible to use Blasius profile for this problem as the flow past a stationary object near a stationary wall. For starting the computation, the whole numerical domain is initialized with zero velocity. Then, the flow enters the domain by the inlet with a constant entrance velocity and turbulent conditions defined above.

4.2 Computational grids

The surface mesh is generated with unstructured triangle faces. The front of the body is meshed with element of 3.5 mm. The roof and the sides are meshed in 4 mm. The rear slanted surface and the vertical base are refined with

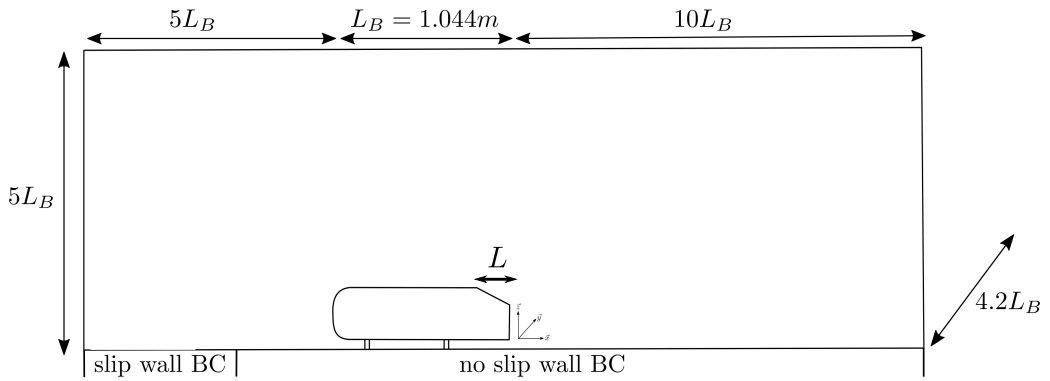

Fig. 4 Schematic representation of the computational domain

respectively 2 mm and 3 mm meshes. The total number of elements on the Ahmed body surface is equal to 315 000. Then, prism layers are extruded from the triangle surface mesh and used for the boundary layer resolution. Then, the whole domain is filled by tetrahedron cells with box refinement in strategic locations of the flow (forebody, underbody and rear slant surface) to capture the separation/attachment phenomenon, as shown with the red line in Fig. 5. Three different grids have been realized. These grids are respectively made of 15, 20 and 30 prism layers, and are called 15l, 20l and 30l thereafter with "l" meaning layers. The name of the grids depends on the prismatic growth as it is one of the most important parameter to accurately predict the flow around the body. Indeed, we will see after that the mesh control in the separation area is essential for the flow prediction while the grid refinement around the body (tetrahedron cells) is less critical. In order to ensure a transition as smooth as possible between prism and tetrahedron cells, the tetrahedron boxes over the slanted surface have been refined carefully such as $L_{ref} = 6$ mm, $L_{ref} = 5$ mm and $L_{ref} = 3$ mm, respectively for 15l, 20l and 30l grids, where L_{ref} represents the edge length of a regular tetrahedron. Tab. 1 gathers all the information concerning the prism layers extrusion: the first layer height h_1, the Δz^+ corresponding value defined as $\Delta z^+ = \frac{u_\tau \times \Delta z}{\nu}$ with u_τ and Δz are respectively the friction velocity and the grid spacing in the vertical direction, the number of prism layers, the Stretch Factor (SF) of prism cells and the total cell number. For the three grids, the total height of prism inflation is kept constant, to ensure that the whole boundary layer is captured by the prism cells. Indeed, the use of tetrahedron cells in the boundary layer would result in numerical diffusion and the deterioration of the solution. The mesh in the rest of the domain is the same, as no major influence over the solution has been observed with grid refinement. In the wake of the vertical base and in the underbody, the L_{ref} values are respectively 10 and 5 mm. The surface mesh is identical between the three grids. A surface grid study, not discussed here, have shown the best results using this surface grid refinement. The surface mesh is built complying with Menter's criterion ($r = \frac{\Delta_{max}}{\delta} > 0.2$), detailed in Sect. 3.2.3. The roof of the body is refined with 4mm edge triangle, and 2 mm at the very end of the roof, just before the transition to the rear slant surface in order to resolve small scales in the separation region. Considering that the boundary layer thickness is equal to 12 and 16 mm respectively at the middle and the end of the roof, the r ratio is equal to 0.29 and 0.11. The criterion is met over a large part of the roof. The violation of the criterion on a small part of the roof, at the very end, is not troublesome. However, surface grid more refined over all the roof induces flow topology modification, with shorter recirculation bubble over the slanted surface.

Table 1 Comparisons of various parameters for the three different grids

Grids	h_1 [mm]	Δz^+	Number of layers	SF	Total cells number [Million]
$15l$	0.025	2	15	1.461	12
$20l$	0.007	0.7	20	1.406	15
$30l$	0.007	0.7	30	1.232	22

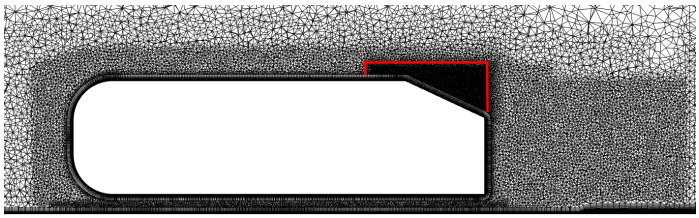

Fig. 5 Mesh in symmetry plane Y0 - the red curve shows the position of the box refinement around the rear surface

In the streamwise and spanwise directions, the mesh is refined as $30 < \Delta x^+ = \Delta y^+ < 250$ for the rear slant, defined as $\Delta x^+ = \frac{u_\tau \times \Delta x}{\nu}$ and $\Delta y^+ = \frac{u_\tau \times \Delta y}{\nu}$ respectively for streamwise and spanwise directions, with a mean value of $\Delta x^+ = \Delta y^+ \approx 120$. These values are quite close to similar studies from Ashton and Revell [3] and Guilmineau et al. [15].

It should be outlined that the comparative study of turbulence models is performed on the finest grid, the $30l$ one. Moreover, the use of structured grid with hexcore cells has been carried out during this work. The authors found globally equivalent results between tetrahedron and hexcore grids. Consequently, this study is carried out using tetrahedron unstructured grids.

4.3 Solver configuration

The results of the simulation presented in this study have been carried out with ANSYS Fluent 16 CFD code [2]. This software uses a 3D finite volume method to solve the incompressible Navier-Stokes equations using a cell-centered data arrangement. A control-volume-based technique is used here. It consists of the division of the domain into discrete control volumes (grid), the integration of the governing equations on the control volume to construct algebraic equations for the discrete equations and the linearization of the discretized equations and solution of the resultant linear equation system. Let us consider the steady-state continuity (10) and momentum (11) equations in integral form:

$$\oint \rho \vec{v} . d\vec{A} = 0 \tag{10}$$

$$\oint \rho \vec{v} \vec{v} . d\vec{A} = -\oint pI . d\vec{A} + \oint \bar{\bar{\tau}} . d\vec{A} + \int_V \vec{F} \, dV \tag{11}$$

where I is the identity matrix, $\bar{\bar{\tau}}$ is the viscous stress tensor and $\vec{F}$ is the force vector.

Equation (10) can be integrated over the control volume and be defined in discrete way as detailed below:

$$\sum_{f}^{N_{faces}} J_f A_f = 0 \tag{12}$$

where J_f is the mass flux through face f. In the same way, equation (11) can be written in discrete form if we only consider the x-momentum equation:

$$a_p u = \sum_{nb} a_{nb} u_{nb} + \sum p_f A.\hat{i} + S \tag{13}$$

where the subscript p and nb refers to the considered cell and the neighbor cells, a_p and a_nb are the linearized coefficients of u and u_{nb}, p_f is the pressure at the face along direction $A.\hat{i}$ and S is a source term. Using this methodology permits to solve the linear equation system created to compute the values of pressure, velocity and turbulence fields.

Convective fluxes are approximated with the use of the second order Bounded Central Differencing (BCD) scheme [21], which consists of a blend between pure central difference scheme, second-order upwind scheme and first-order upwind scheme. Diffusive terms are discretized with second order central difference scheme. The pressure values at the faces are discretized using second order central differencing scheme. Gradients are computed using the average of the nodal values on the considered face. The SIMPLEC algorithm is used for pressure/velocity coupling. The temporal resolution is achieved with second order implicit scheme, ensuring the numerical scheme to be unconditionally stable. For hybrid RANS/LES methods, as in LES computations, low dissipation schemes are required to allow the resolution of the resolved 3D scales. Classical second order upwind scheme would annihilate the turbulent structures in the flow. On the contrary, pure Central Differecing (CD) scheme can be unstable or produce unphysical wiggles in the solution. Even if BCD scheme is slightly more dissipative than CD scheme, it is the optimal choice.

In computational simulations, the time step can be related to a non dimensional number, the Courant-Friedrichs-Lewy (CFL) number. This number is defined as $CFL = \frac{V_\infty \Delta t}{\Delta x}$ with V_∞ the free stream velocity, Δt the time step and Δx the grid spacing. Beyond, flow information can be canceled. Generally, especially for explicit time integration, a CFL lower than one is required for scheme stability. In practice, even with the use of implicit time integration, which is unconditionally stable, a CFL close to one is also advised. In this work, two different CFL are studied: one around 1 and one around 3 to reduce computational time and with the perspective to apply the SRS method on a real car with bigger mesh and consequently more costly numerical resources. The $CFL = 1$ is associated to $\Delta t = 1.5 \times 10^{-5}$ s and the $CFL = 3$ to $\Delta t = 5 \times 10^{-5}$ s, leading to respectively non-dimensional time step $\Delta t.V_\infty/L_B = 0.0005$ and $\Delta t.V_\infty/L_B = 0.002$. The computations were run for a total of 77 convective transit times defined as $T.V_\infty/L_B$, with $T = 2$ seconds of physical time. The time-averaging process was started after 38 transit times (1 second of physical time), ensuring the relevance of the averaged quantities. In addition, all of the post-processed variables in the below sections (C_d, C_l, C_p, U_x, k, ν_t/ν, f_d and Q) are time-averaged.

5 Numerical study around the sharp edges Ahmed body

5.1 Comparisons of turbulence models - RANS, SAS, DDES and SBES models

Hereafter, the numerical performances of SST RANS (steady computation), SAS, DDES and SBES turbulence models are discussed. The comparisons are realized on the finest grid ($30l$), with a standard $CFL = 1$. This grid was chosen after a grid independence verification for all turbulence models.

The comparisons of drag (C_d) and lift (C_l) coefficients and the recirculation bubble length L_R, between experiments and numerical simulations are summarized in Tab. 2. The recirculation bubble length L_R, defined as the ratio between the recirculation bubble length over the rear slanted surface length, is equal to 78% in experiments. The length L_R is computed based on the visualization of wall shear stress over the rear slanted surface. The positive bifurcation lines indicates the closure of the recirculation bubble. The length L_R is computed in the symmetry plane $Y^* = 0$. This result is cross-checked using the streamlines in the symmetry plane, to detect the reattachment position of the flow. Fig. 7 displays the mean wall shear stress over the back of the body for the four turbulence models considered. The demarcation of the closed recirculation bubble is observed with the red curve from computational results. The black dashed line represented the length of the recirculation bubble from experiments. The yellow curve represents the position of the longitudinal vortices over the slanted surface, very close for the three hybrid turbulence models.

First of all, the prediction of both C_d and C_l coefficients for SST RANS model is highly underestimated. This clearly indicates a massive flow separation on the rear slanted surface, as observed in Fig. 7 (a), similar to the flow topology of the 35° Ahmed body. This flow behavior confirms the inability of RANS models to accurately predict the closed recirculation bubble on the rear window, as explained in the introduction. For such a flow, more sophisticated turbulence models are required with more flow structures resolution to accurately predict the separation/reattachment position over the body.

Even if the SAS shows an accurate prediction regarding drag and lift coefficients, this result must be put in perspective as the SAS flow topology is less representative compared to the experimental flow. The length of the recirculation bubble is highly overestimated (see Fig. 7 (b)), equal to 99% of the rear window length. In fact, a focus on different parts of the body (mainly the rear slanted and the vertical base surfaces) show that SAS coefficients accuracy are due to errors compensation. DDES model gives very good prediction for drag coefficient,with an error equal to -0.5%. The length of the recirculation bubble is accurately predicted, with 85% compared to 78% in experiments (see Fig. 7 (c)). The time histories of drag and lift coefficients are shown in Fig. 6 for DDES model. The drag evolution is stable during the computation from 0.6 s and comprise between 0.34 and 0.36 with a mean value of 0.354. The lift evolution is more fluctuating, comprise between 0.3 and 0.4 with a mean value of 0.334. This plot shows that averaging variables between 1 to 2 seconds is reliable. SBES model predicts both drag and lift coefficient with respectively -4.2% and 5.4% errors. Moreover, the flow separation is highly under-estimated with this model, leading to $L_R = 53\%$ (see Fig. 7 (d)). Based on this analysis, DDES model prediction is superior to the others turbulence models.

Table 2 Comparisons of drag and lift coefficients and recirculation bubble length between experiments and SST RANS, SAS, DDES and SBES models for the grids $30l$ and $CFL = 1$

Models	C_d	$\Delta C_d\,[\%]$	C_l	$\Delta C_l\,[\%]$	$L_R\,[\%]$
Exp. [41]	0.356	± 0.5	0.311	± 1	78
SST	0.292	-17.9	0.103	-66.9	-
SAS	0.355	- 0.3	0.298	- 4.0	99
DDES	0.354	- 0.5	0.334	7.4	85
SBES	0.341	- 4.2	0.328	5.4	53

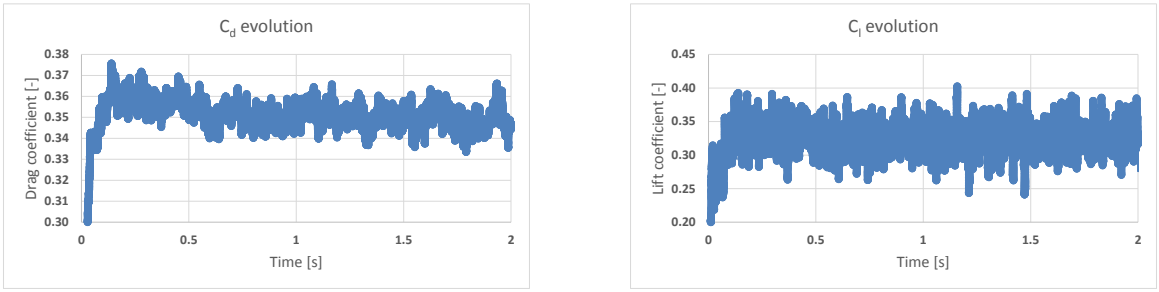

(a) C_d (b) C_l

Fig. 6 Drag and lift coefficient evolution over 2 seconds of physical time for DDES computation

Fig. 8 displays mean streamwise velocity U_x^* profiles along the rear slanted surface for planes (a) $Y^* = 0$ and (b) $Y^* = 0.5$. In the symmetry plane, the best prediction of the flow with DDES is clearly observable on the velocity profiles. Due to the close reattachment zone between experiments and DDES, a good agreement is obtained on the rear slant surface and in the wake of the body (not shown here) in the symmetry plane. The quick reattachment of the SBES model is clear, as the formation of a boundary layer is observable at the location $X^* = -0.5$. On the contrary, the SAS reattachment zone is only situated at the end of the rear slant surface, so low velocity is notable at all locations of velocity measurement (in the recirculation region). The same trend is observable in the plane $Y^* = 0.5$. Globally, these results indicate again that the DDES model accurately predicts the shape of the closed recirculation bubble.

The evolution of mean modeled k_m and total turbulent kinetic energy k_t are displayed in Fig. 9 for planes $Y^* = 0$ and $Y^* = 0.5$. The same scale is used for the plots, for greater clarity and direct comparison between the different turbulent kinetic energy contributions. The mean modeled k_m values for SAS model is highly larger compared to DDES and SBES for both planes (figures (a) and (b)). It clearly shows that the switch to resolved contents is delayed with SAS, especially on the first half of the rear slanted surface. This RANS behavior leads to an over prediction of the recirculation bubble length. Very low level of modeling is observed with both DDES and SBES models. The switch from RANS to LES resolution, just after separation, is very fast. The contributions of the mean resolved k_r is then added to the modeled one to display the mean total k_t on figures (c) and (d).

In the symmetry plane (c), the peak of k_t emanating from the shear layer separation on the top of the rear slanted angle is respectively under-estimated (indicating low level of k_r) and over-estimated in the first three measurement locations (from $X^* = -0.9$ to $X^* = -0.7$) for SAS and SBES models. This energy behavior leads to longer and shorter recirculation length respectively for SAS and SBES models. As already shown in previous studies [3] and

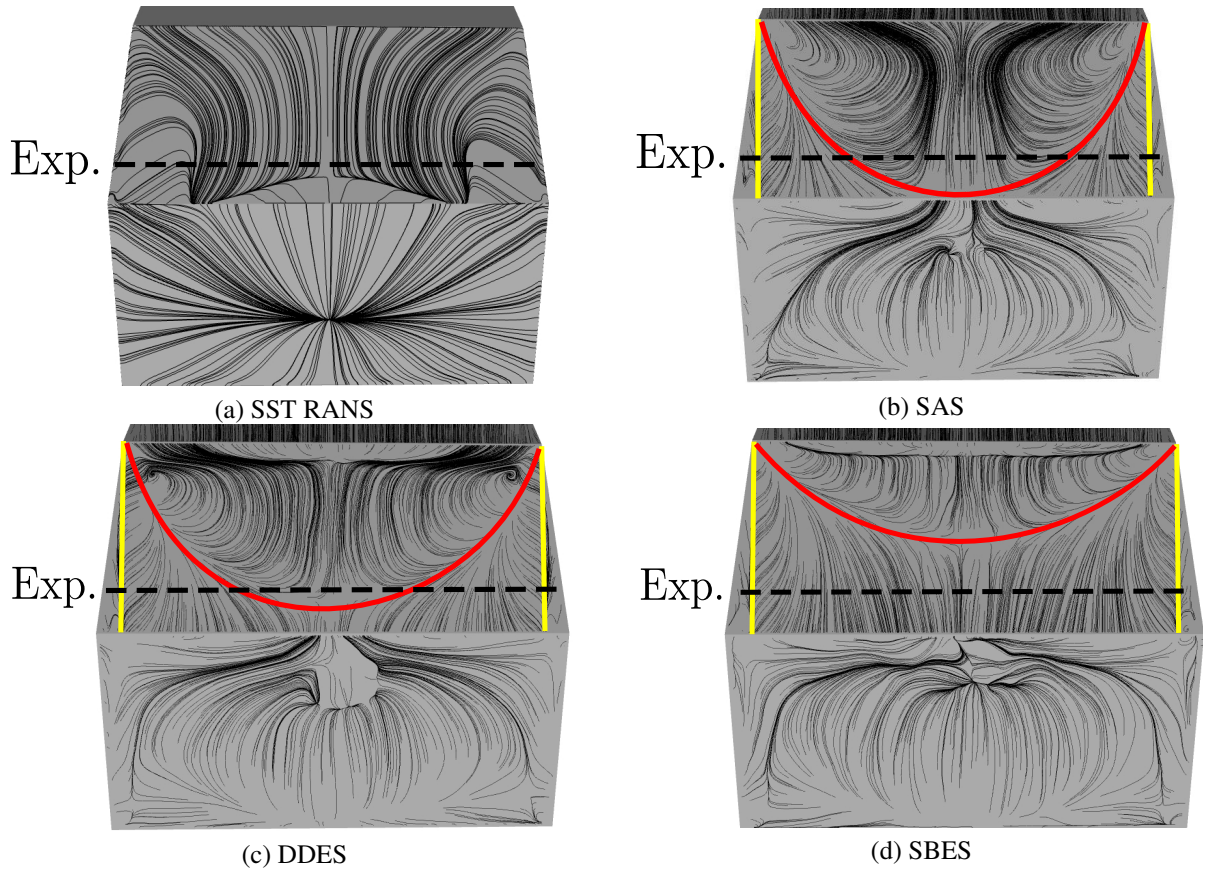

(a) SST RANS (b) SAS

(c) DDES (d) SBES

Fig. 7 Representation of mean wall shear stress over the back of the body for SST RANS, SAS, DDES and SBES turbulence models for the 30*l* grid - red line indicates the shape of the closed recirculation bubble and yellow line the position of longitudinal vortices over the rear slant surface from computations - the dashed black line shows the position of the reattachment area from experiments

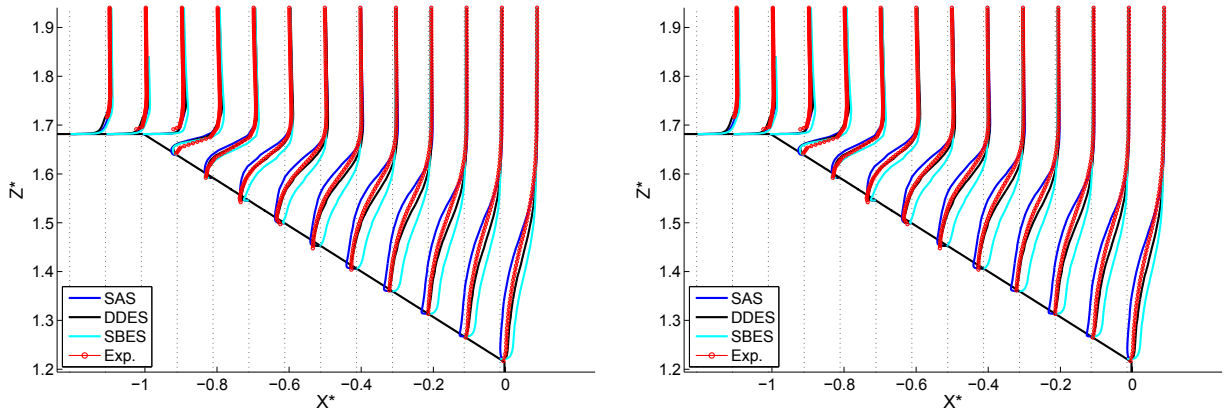

(a) U_x^* - $Y^* = 0$ (b) U_x^* - $Y^* = 0.5$

Fig. 8 Evolution of mean streamwise velocity U_x^* (a) in the symmetry plane $Y^* = 0$ and (b) plane $Y^* = 0.5$ over the slanted surface for the 30*l* grid

[37], the higher the turbulent kinetic energy and as a consequence the higher the turbulent mixing are, the shorter the recirculation bubble length and vice versa. The peak of k_t is very well predicted for $X^* = -0.9$ to $X^* = -0.8$ with DDES model. The intensity of energy is globally well predicted all over the rear slant surface, even though the Z* location is slightly under-estimated. In the eccentric plane $Y^* = 0.5$ (d), the same conclusions can be drawn for the SAS model. The thickness of the recirculation bubble is highly overestimated compared to experiments on the whole rear surface.

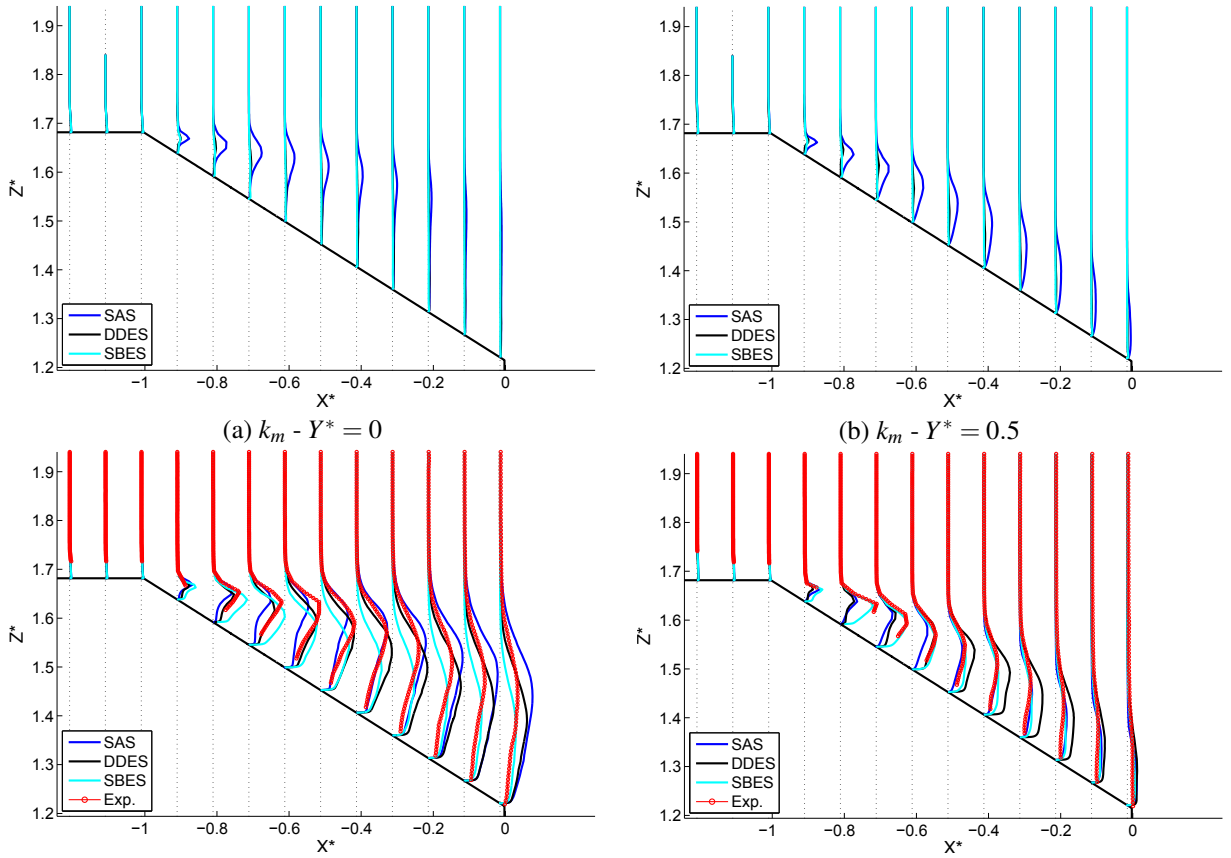

(a) k_m - $Y^* = 0$ (b) k_m - $Y^* = 0.5$

(c) k_t - $Y^* = 0$ (d) k_t - $Y^* = 0.5$

Fig. 9 Evolution of mean modeled turbulent kinetic energy (a) in the symmetry plane $Y^* = 0$ and (b) plane $Y^* = 0.5$ and mean total turbulent kinetic energy (c) in the symmetry plane $Y^* = 0$ and (d) plane $Y^* = 0.5$ over the slanted surface for the $30l$ grid

To confirm previous analyze of k quantities, the mean ratio of the turbulent viscosity to the molecular viscosity ν_t/ν is shown in Fig. 10 at three locations: (a) $X^* = -0.91$, (b) $X^* = -0.51$ and (c) $X^* = -0.11$ where $X^* = -1$ corresponds to the transition roof/rear surfaces and $X^* = 0$ the end of the rear surface. The quantity ν_t/ν reflects the quality resolution of turbulence modeling based on the mesh. Lower values mean more resolution of the flow scales as high value damps out the turbulence. For the three plots, the same interfiling is observable. SAS levels of viscosity ratio are higher than DDES, respectively higher than SBES. The high SAS values confirm the high level of k_m leading to the overestimation of the separation on the rear slant surface. DDES values are low, meaning that the model is resolving LES contents of the flow. By construction, the eddy viscosity level is very low for the SBES model, which is confirmed here [2].

From these results, the recirculation bubble length can be directly linked to turbulent kinetic energy level. The longer recirculation from SAS computation compared to experiments is explained by under-estimated total turbulent kinetic energy level combined with high modeled energy compared to DDES and SBES models in the separation area. This is one of the shortcomings of SAS model: the transition from RANS to the resolution of LES contents is slow. In such a case, where there is no massive flow separation, DDES model is advised over SAS. Very low level of modeling is observed for SBES with higher level of k_t compared to experiments. This leads to a dramatically shorter recirculation length compared to experiments. This situation can be explained by the inherent formulation of SBES model with very

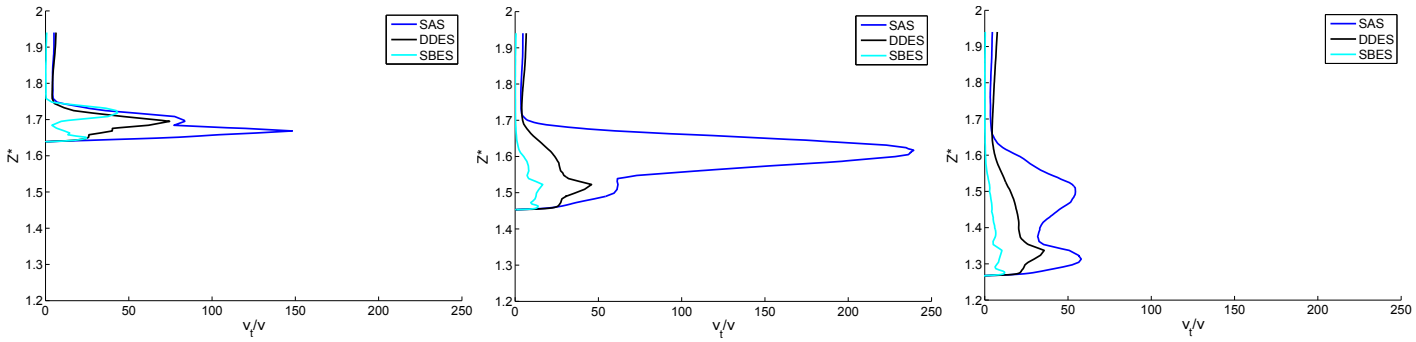

(a) $X^* = -0.91$ - $Y^* = 0$ (b) $X^* = -0.51$ - $Y^* = 0$ (c) $X^* = -0.11$ - $Y^* = 0$

Fig. 10 Evolution of mean viscosity ratio ν_t/ν for (a) $X^* = -0.91$ (just after separation, at the beginning of the rear slant surface), (b) $X^* = -0.51$ (in the middle of rear slant surafce) and (c) $X^* = -0.11$ (at the end of rear slant surface) over the slanted surface for the $30l$ grid in the symmetry plane $Y^* = 0$

low eddy viscosity, which reduces the damping of turbulent structures and also speed up the transition from RANS to LES contents. Finally, the k_t is well predicted by DDES leading to almost perfect prediction on the recirculation bubble length.

This study clearly indicates the superiority of the DDES model over SAS and SBES formulations on the global flow prediction (aerodynamic coefficients and recirculation bubble length). As a consequence, SST DDES is the reference model for more detailed studies in the following section.

5.2 Computational results with SST DDES

This section is devoted to a detailed study of numerical space and time parameters and their effects on the DDES approach simulations. First, the grids detailed in Sect. 4 are reviewed. Then, the time step is modified to study the grid sensitivity and reduce as much as possible the computational time without deteriorating computational results. The box refinement over the slanted surface is examined in order to find the best grid size to characterize flow separation area. Finally, the physics of the flow is studied with the best setup, based on previous results.

5.2.1 Grid refinement in the boundary layer

The DDES model is studied on the three grids described in Sect. 4, with a $CFL = 1$. The comparisons of drag C_d and lift C_l coefficients and the recirculation bubble length L_R, between experiments and numerical simulations are

Table 3 Comparisons of drag and lift coefficients and recirculation bubble length between experiments and DDES for the three different grids with $CFL = 1$

Models	C_d	$\Delta C_d\,[\%]$	C_l	$\Delta C_l\,[\%]$	$L_R\,[\%]$
Exp. [41]	0.356	± 0.5	0.311	± 1	78
$15l - CFL = 1$	0.367	3.1	0.333	7.1	95
$20l - CFL = 1$	0.365	2.5	0.333	7.1	96
$30l - CFL = 1$	0.354	- 0.5	0.334	7.4	85

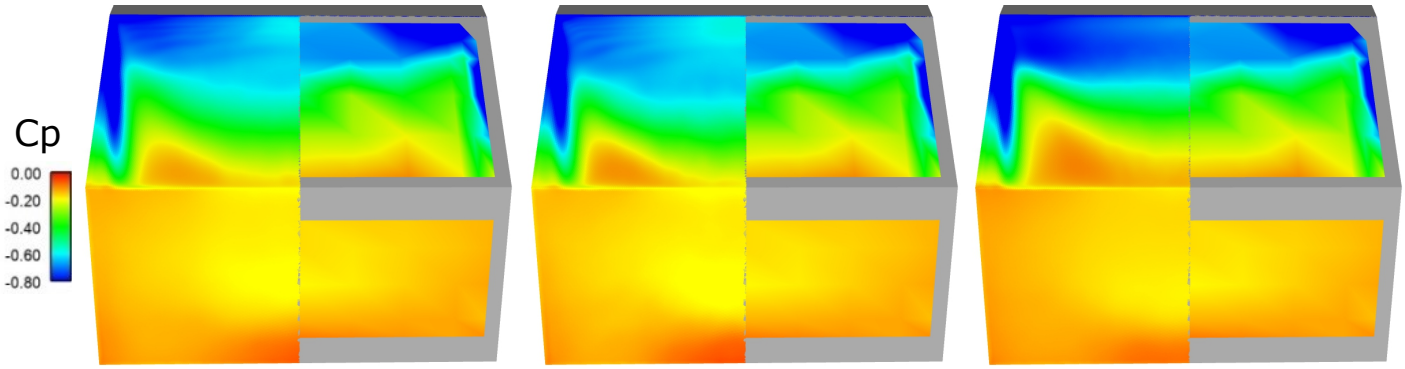

(a) 15l grid (b) 20l grid (c) 30l grid

Fig. 11 Representation of mean C_p over the back of the body for the 15l, 20l and 30l grids - left part of the picture corresponds to the simulation result and the right part to the experimental result

summarized in Tab. 3. As mentioned previously, the recirculation bubble length L_R is equal to 78% in experiments. The three grids show a satisfactory prediction for the drag coefficient, with prediction error between -0.5% and 3.1%. More discrepancy is observed concerning lift coefficient, around 7%. Both 15l and 20l grids lead to an overestimation of the length of the recirculation bubble (around 95%), and the best bubble length prediction is obtained for the 30l grid with $L_R = 85\%$. It should be outlined again that a precise prediction of the bubble length recirculation as well as the drag coefficient are the main criteria for this convergence study because they are two essential features of this flow behavior.

Fig. 11 displays the C_p coefficients on the back of the body for the three grids. The left part of the picture corresponds to the simulation results and the right part to the experimental measurements. The 15l and 20l grids show the same behavior with higher C_p values in the upper part of the rear slanted surface. This lower depression is caused by the longer recirculation bubble length. Very good agreement is obtained with the 30l grid. The footprint of the longitudinal vortices is observable along the edges of the rear window with very low C_p values. From experimental and numerical results, a pressure recovery is clearly observable along the rear slant surface: at the onset of the separation, C_p values are low, around -0.8; moving downward the rear slant surface, the pressure increases as the bubble recirculation is thinner and the flow is about to reattach on the surface.

Fig. 12 gives a closer look in the evolution of C_p along the symmetry plane $Y^* = 0$ and the offset plane $Y^* = 0.9$. For the two locations, the C_p evolution is very well predicted for both computations along the vertical base, from $S^* = 0$ to $S^* = 0.5$. The C_p evolution along the rear slanted is observable for $S^* = 0.5$ to $S^* = 1$. In the plane $Y^* = 0$, around the separation area due to sharp edges at the end of the roof, for $0.8 < S^* < 1$, the C_p values are very low. The 30l shows the best prediction compared to experiments. For $0.5 < S^* < 0.8$, a pressure recovery is observable in all cases, with perfect match for the 30l grid. In the $Y^* = 0.9$ plane, both case show good agreement compared to experiments.

Mean streamwise velocity U_x^* profiles, directly link to the shape of the recirculation area and C_p coefficients, are plotted in Fig. 13 in the centerline and at locations (a) $X^* = -1.2$ on the roof, (b) $X^* = -0.6$ and (c) $X^* = -0.3$ over the slanted surface and (d) $X^* = 0.2$ in the wake of the body. At the very end of the roof, on plot (a), the velocity profiles in the boundary layer for 15l and 20l grids are similar. For the 30l grid, the velocity is moderately overestimated and a

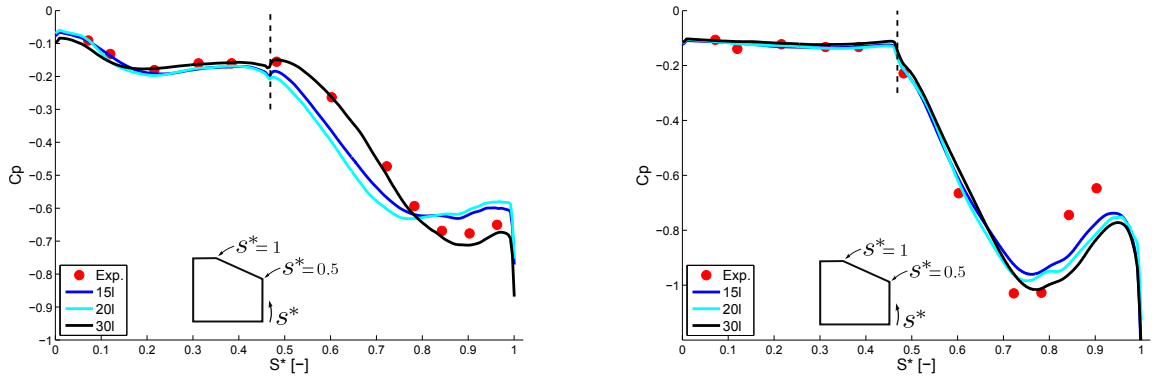

(a) $Y^* = 0$ (b) $Y^* = 0.9$

Fig. 12 Evolution of C_p along the rear slanted surface and the vertical base in the planes (a) $Y^* = 0$ and (b) $Y^* = 0.9$, for the $15l$, $20l$ and $30l$ grids with $CFL = 1$

modification in the profile is depicted, mainly due to the f_d function values as will be explained later. The velocity in the outer part of the boundary layer is slightly over-estimated from computations compared to experiments. Over the backlight, plots (b) and (c), the mean streamwise velocity is under predicted for both $15l$ and $20l$ grids, while slightly overestimated for $30l$ grid, even though a fair prediction of the flow velocity over the rear slanted surface. In the wake, on plot (d), the finest grid shows the best prediction of the flow in the wake of the body.

A good indication of the grid resolution is the ratio of the turbulent viscosity to the molecular viscosity ν_t/ν. Fröhlich et al. [12] showed that this ratio should be close to 1 as much as possible. However, this will require a huge grid refinement. Fig. 14 displays the mean viscosity ratio for the three grids. The viscosity is reduced from $15l$ to $30l$ grid, especially over the rear slant surface. This result confirms that more small structures are resolved with grid refinement. The ratio reaches values around 30 over the slanted surface and 50/60 in the wake for the $30l$ grid. This result is similar to Ashton and Revell work [3] where the authors reported values close to 50 in the initial separation region and 40 further downstream the body. The results from the $30l$ grid are totally satisfactory meaning that the grid refinement is fine enough for this mesh.

The behavior of the DDES model is now studied. The switch between RANS and LES modes of the DDES model can be examined through the evolution of the shielding function f_d (Eq. (7)). This function is built to protect the boundary layer against LES intrusion and shown in Fig. 15 in the plane $Y^* = 0$. The function has globally the same values in the plane $Y^* = 0.5$, not shown here. When $f_d = 0$ (blue color), the models acts in RANS mode. When $f_d = 1$ (red color), the model switches to LES resolution. The whole boundary layer is protected for the $15l$ and $20l$ grids. For the $30l$ mesh, the LES penetrates the boundary layer into two prism cells as observed in Fig. 16, where a closer look is done at the location $X^* = -1.2$ and $Y^* = 0$, at the end of the body roof. As mentioned previously by Menter and Kuntz [33], the flow separation is governed by the sharp edges of the body and not by adverse pressure gradient. For this reason, it is not problematic if the DDES limiter (i.e the function f_d) allows LES resolution in the upper part of the boundary layer. Grid-induced separation is not expected in this particular case. Moreover, these observations clearly indicate that LES intrusion in the boundary layer increases while refining the grid in the boundary layer. For a case with

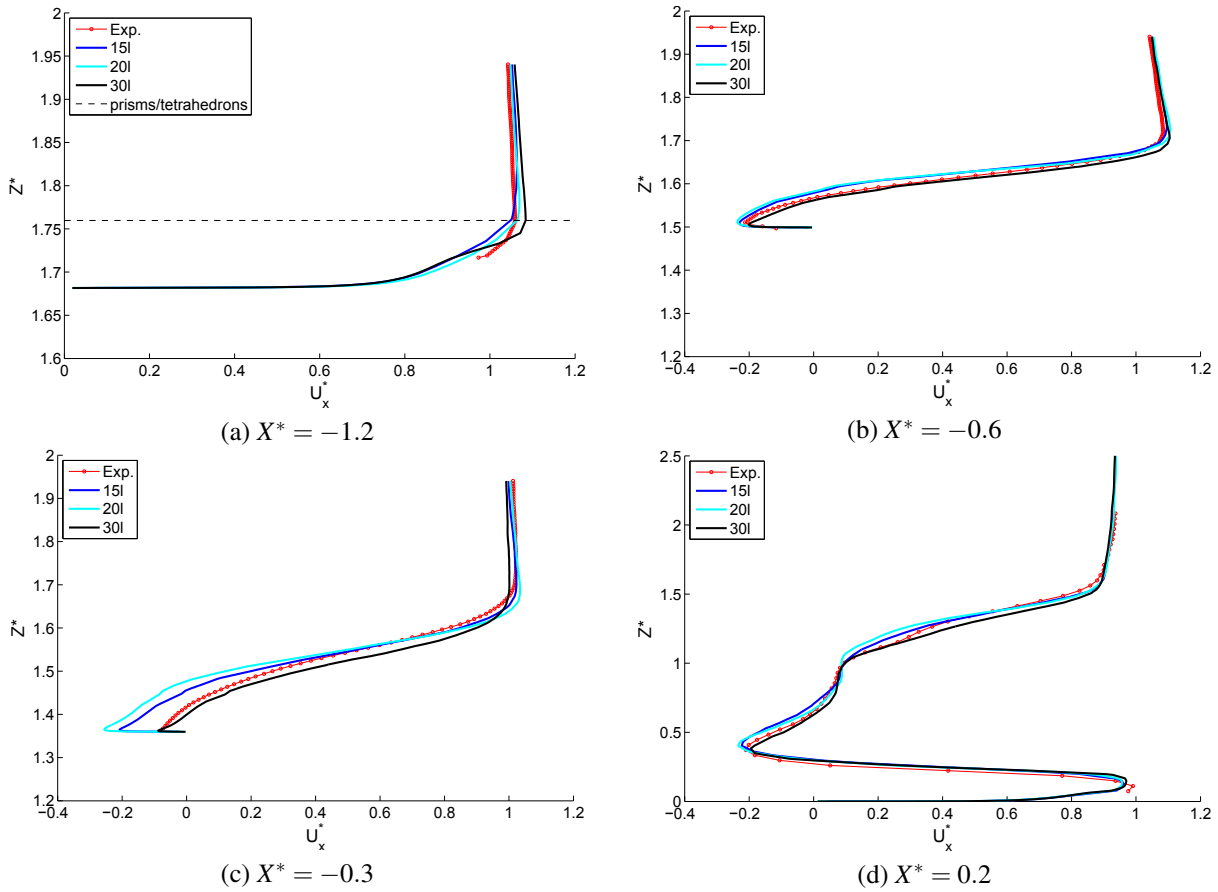

(a) $X^* = -1.2$ (b) $X^* = -0.6$

(c) $X^* = -0.3$ (d) $X^* = 0.2$

Fig. 13 Profiles of mean streamwise velocity U_x^* for $15l$, $20l$ and $30l$ grids at the locations $X^* = -1.2$, $X^* = -0.6$, $X^* = -0.3$ and $X^* = 0.2$ in the symmetry plane of the body $Y^* = 0$

rounded edges where the separation is driven by the adverse pressure gradient, special care will be necessary to control the protection of the boundary layer. Besides, grid refinement over the slanted surface reduce the grey-area of the model (area in green color reduced). The transition from RANS to LES resolution is faster, allowing better resolution of small scales. Moreover, the shape of the velocity profile in the boundary layer for the $30l$ grid, observed before in Fig. 13, is correlated to the f_d function, as observed in Fig. 16. Without LES intrusion in the boundary layer, this phenomenon is not observed for both $15l$ and $20l$ grids. Despite this discrepancy due to the LES intrusion in the boundary layer, from the overall point of view, the $30l$ case behaves more accurately (regarding drag and lift coefficients and the size of the closed recirculation bubble) than the $15l$ and $20l$ cases and clearly indicate the superiority of the $30l$ grid over the two others meshes. In order to precisely capture the flow structure with LES resolution, a mesh refined as the $30l$ one is required. The $30l$ grid is referred as the referenced mesh in the next study.

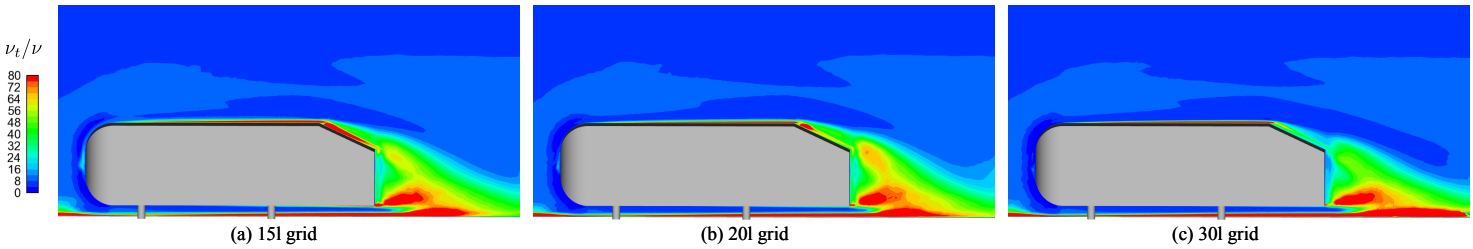

(a) 15l grid (b) 20l grid (c) 30l grid

Fig. 14 Evolution of mean ν_t/ν for $15l$, $20l$ and $30l$ grids in the symmetry plane $Y^* = 0$

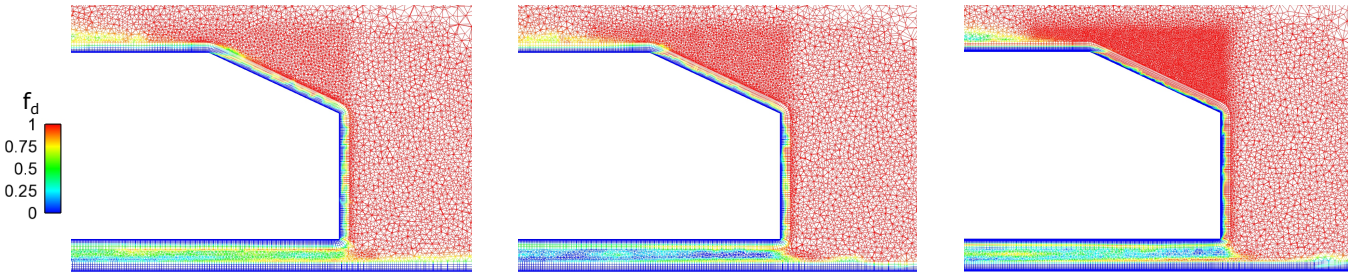

(a) 15l grid (b) 20l grid (c) 30l grid

Fig. 15 Representation of the shielding function f_d for the 15l, 20l and 30l grids in the symmetry plane $Y^* = 0$

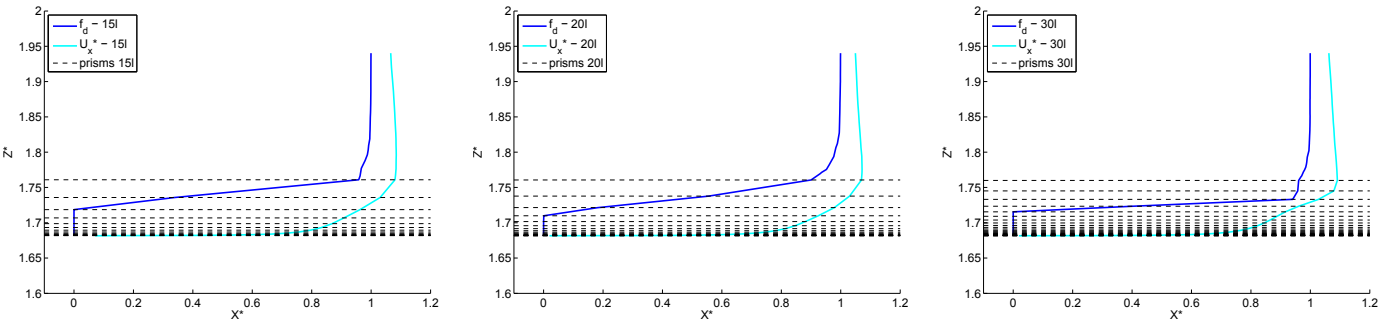

(a) 15l grid (b) 20l grid (c) 30l grid

Fig. 16 Representation of the shielding function f_d (color blue) and mean streamwise velocity U_x^* (color cyan) with the prism layers extrusion (color black) for 15l, 20l and 30l grids at the location $X^* = -1.2$ and $Y^* = 0$

5.2.2 Time step influence

In this section, the CFL number is increased from 1 to 3 near the separation of the shear layer. The main target is to study the influence of the time step on the flow separation and resolution. Moreover, the computational cost is reduced by three for a $CFL = 3$, which is very interesting in the perspective of the DDES model use on a real car. The comparisons of drag and lift coefficients and the recirculation bubble length L_R, between experiments and numerical simulations are summarized in Tab. 4. It is noticed that by increasing the CFL number, the length of the recirculation is shorter, from 85% to 75%, very close to the 78% in experiments. The same observation is done on drag and lift coefficients with a better prediction on the lift with higher CFL. This result confirms that the closed recirculation bubble over the rear slanted surface is mainly responsible for both drag and lift. The reason for that is twofold. First, a shorter recirculation leads to higher C_p absolute values over the rear slanted surface (in both x and z directions, then directly reducing drag and lift contributions). Second, the rear slant closed bubble directly influences the upper recirculation along the vertical base. Indeed, a shorter recirculation bubble will lead to a longer 3D recirculation in the wake, and vice versa. This physical behavior of the flow is clearly explained in Sect. 6.1.2 in Fig. 28, where the streamlines between two Ahmed body configurations are depicted and illustrate this phenomenon. If the structure is pushed downwards, C_p absolute value is higher on the vertical base. Consequently, the drag is lower. As a consequence, a shorter recirculation leads to a reduction of drag and lift.

Table 4 Comparisons of drag and lift coefficients and recirculation bubble length between experiments and DDES for the $30l$ grid

Models	C_d	$\Delta C_d\,[\%]$	C_l	$\Delta C_l\,[\%]$	$L_R\,[\%]$
Exp. [41]	0.356	± 0.5	0.311	± 1	78
$30l - CFL = 1$	0.354	- 0.5	0.334	7.4	85
$30l - CFL = 3$	0.347	- 2.5	0.323	3.9	75

Fig. 17 displays mean streamwise velocity U_x^* profiles along (a) the rear slanted surface and (b) in the wake of the body in the symmetry plane $Y^* = 0$. Globally, the velocity plots are similar. Due to shorter recirculation for the $CFL = 3$ case, higher velocities are noticeable on the rear slant surface compared to $CFL = 1$. In the wake of the Ahmed body, both cases show very good agreement with experiments. Even though the recirculation length is slightly modified, the flow topology remains identical between the two cases which outlines the low influence of the CFL number on this case as the solver is implicit.

The modification of the recirculation length can be explained by giving a closer look on the longitudinal vortices. It is well known that an interaction occurs between the longitudinal vortices and the closed recirculation bubble over the rear slanted surface. The maximum of Q criterion and minimum of C_p are detected in cross flow planes every $X^* = 0.1$ along the rear window, in order to detect the center core of the vortices and the evolution of these quantities at these locations. Fig. 18 details the evolution of (a) Q criterion and (b) C_p coefficients in the center core of the longitudinal vortices. $X^* \in [-1,0]$ represents the evolution of the vortices over the slanted surface. Based on Q criterion evolution, it is clearly noticeable that the vortices are more energetic for the larger $CFL = 3$ case compared to the smaller $CFL = 1$ case. The same observation is done with the C_p, with lower C_p values in the center core of the vortices for $CFL = 3$. The more energetic the longitudinal vortices are, the shorter the recirculation bubble length is.

Fig. 19 shows the evolution of C_p along the rear slanted surface in the planes (a) $Z^* = 1.64$, (b) $Z^* = 1.49$ and (c) $Z^* = 1.34$, for $Y^* \in [0;0.97]$ (right part of the rear windows when looking from behind). In the upper part of the rear window (plot (a)), the footprint of the longitudinal vortices is clearly seen for $Y^* \in [0.9;0.97]$, and give very low C_p for $CFL = 3$ ($C_p^{min} = -1.36$) compared to $CFL = 1$ ($C_p^{min} = -1.06$), which confirms the previous analysis based in Fig. 18 (a). Due to the vortices influence, for $Y^* \in [0.5;0.97]$, the $CFL = 3$ case shows a slightly better agreement with experiments. The same argument is valid for the $Z^* = 1.49$ on plot (b). A good pressure recovery is observed, very close to experiments, as the length of the bubble recirculation is closer from experiments ($L_R = 78\%$) with $CFL = 3$ ($L_R = 75\%$). In the lower plane (plot (c)), the C_p values are closer to experiments with $CFL = 1$. It can be highlighted that C_p values are slightly better with CFL=1 around the symmetry plane. However, the recirculation length is overestimated (85% against 78% in experiments). With $CFL = 3$, Cp are slightly less predictive around the symmetry plane but the recirculation length is better predicted (75% against 78% in experiments). A small difference in the experimental Cp probe positions may explain either the better C_p prediction or the longer recirculation length for the $CFL = 1$ case.

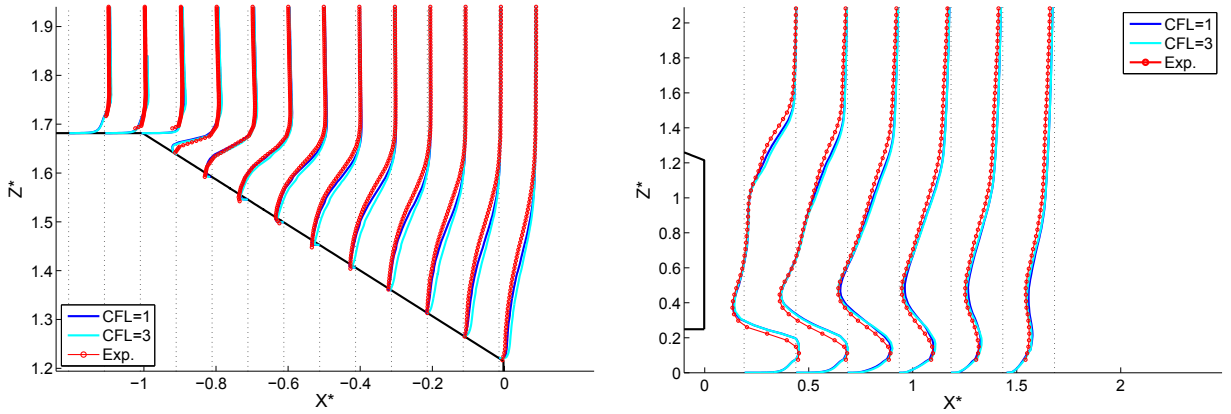

(a) U_x^* - $Y^* = 0$ - rear slanted surface (b) U_x^* - $Y^* = 0$ - wake

Fig. 17 Evolution of mean streamwise velocity U_x^* (a) in the symmetry plane $Y^* = 0$ and (b) plane $Y^* = 0.5$ over the slanted surface for the $30l$ grid

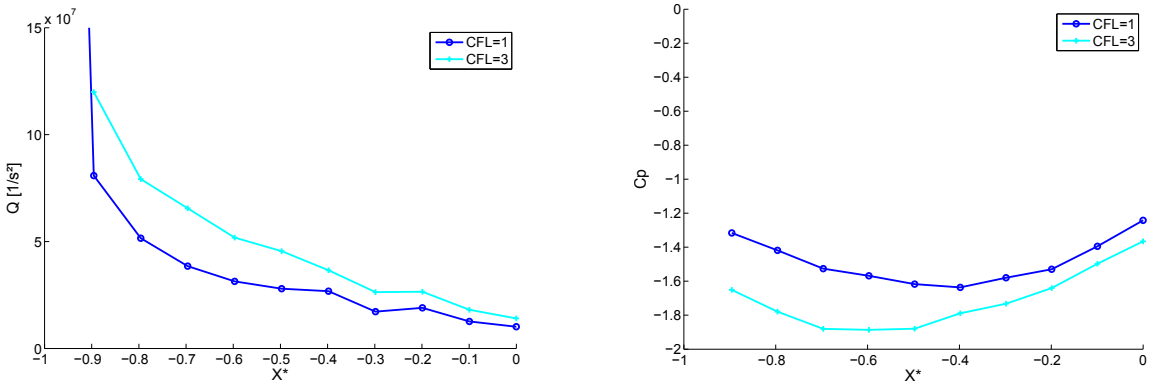

(a) Q criterion (b) C_p

Fig. 18 Representation of (a) maximum of Q criterion and (b) minimum of C_p coefficients in the center core of the longitudinal vortices for the $30l$ grid with $CFL = 1$ and $CFL = 3$

The evolution of the longitudinal vortices is now studied in order to understand their influence on the closed recirculation bubble. Krajnovic and Davidson [27] were the first to meticulously detail the onset mechanism of the vortices. The authors showed that the vortices are in reality composed of three swirling structures, comparable to a gearwheel mechanism. Then, Jermann [22] confirmed the previous authors observations based on a Stereo PIV analysis.

As shown by Jermann [23], the vortices can be described using a set of different angles, depicted in Fig. 20. The α and β angles represent the evolution of the vortices in the (x,z) plane (a), while θ angle is for plane (y,z) (b). Tab. 5 compares the computed angles from computations to experiments. A very good accuracy is obtained regarding experiments results for α and β angles. The angle θ is 2 degrees larger compared to Jermann's experiments. However, it is more coherent with Lehugeur et al. [29] and Thacker [49] experimental results, respectively equal to 7° and 6.2°. The θ angle directly influences the shape of the recirculation area. As observed, the angle is higher for $CFL = 3$ case compared to $CFL = 1$ case, meaning that the longitudinal vortices roll up nearer to the center of the body, bordering the closed recirculation. It may explain the shorter recirculation area over the rear slanted surface for the $CFL = 3$ case. However, it is not easily understandable why the longitudinal vortices are stronger for the higher CFL case.

Globally, velocity profiles are in better agreement with experiments for the $CFL = 1$ case. However, C_p coefficients are slightly closer to the $CFL = 3$. These small discrepancies could come from experiments or numerical results. The

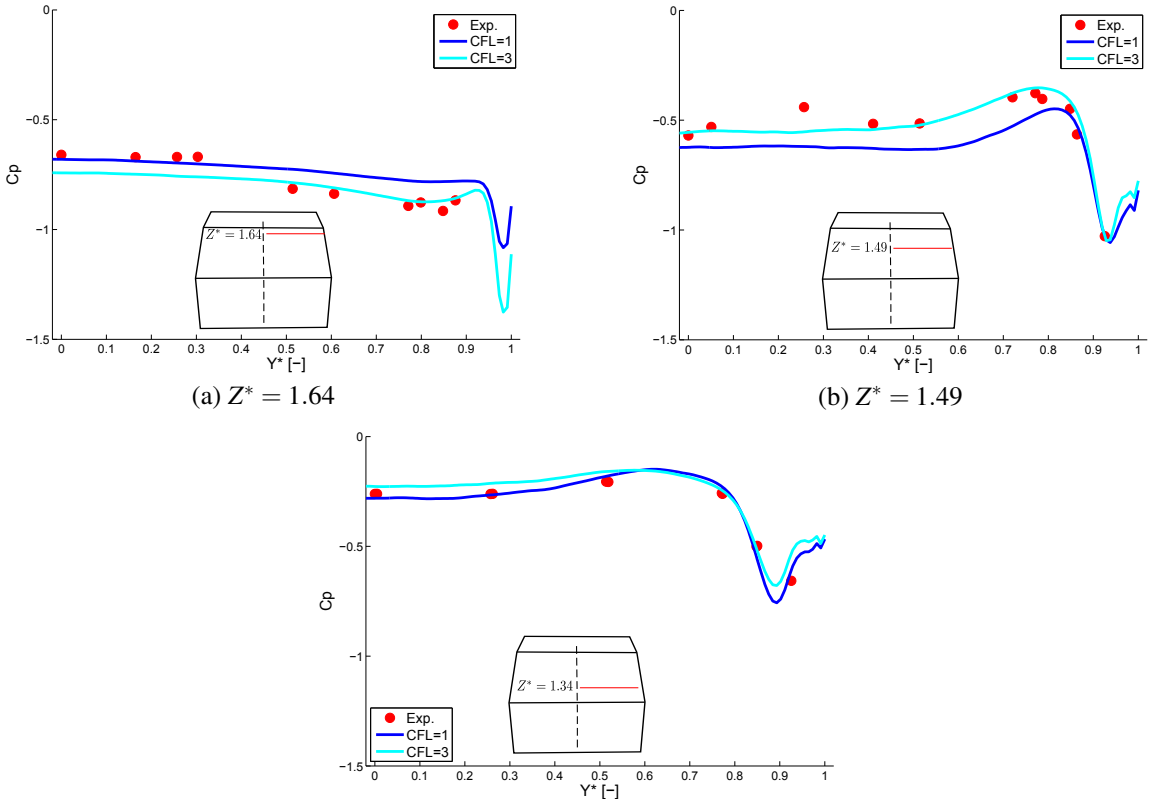

(a) $Z^* = 1.64$ (b) $Z^* = 1.49$

(c) $Z^* = 1.34$

Fig. 19 Evolution of C_p coefficients along the rear slanted surface in the planes (a) $Z^* = 1.64$, (b) $Z^* = 1.49$ and (c) $Z^* = 1.34$, for the $30l$ grid with $CFL = 1$ and $CFL = 3$

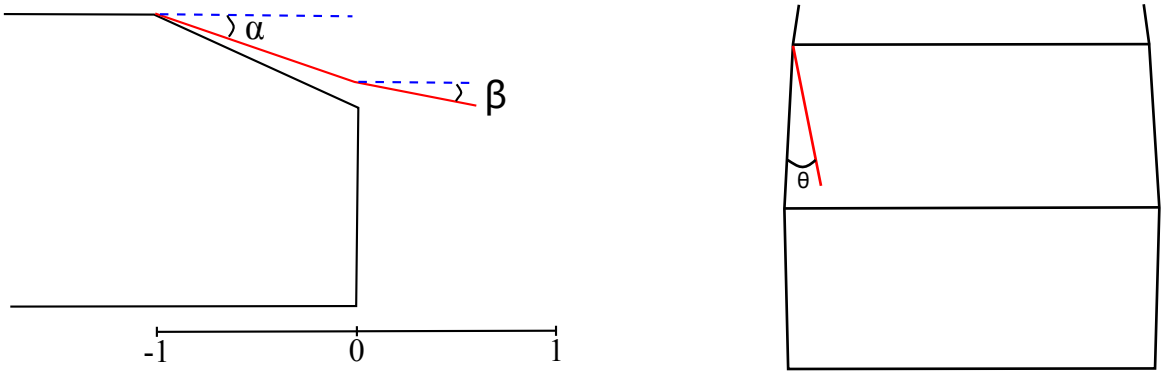

(a) plane (x,z) (b) plane (y,z)

Fig. 20 Representation of the characteristic angles α, β and θ of the longitudinal vortices around the back of the body

results highlight that despite the difficulties to perfectly catch this complex flow on the rear slanted surface, the hybrid methods offers an accurate numerical simulation and for both CFL cases, a very good agreement is obtained compared to experiments (C_d and C_l coefficients, velocity, C_p, longitudinal vortices evolution). This study shows that using an implicit solver, a $CFL = 3$ is enough to provide very good results and save precious computational time and cost.

Table 5 Evolutions of the characteristic angles α, β and θ of the longitudinal vortices around the back of the body for the $30l$ grid - experiments from Jermann [23]

Configurations	$\alpha[^\circ]$	$\beta[^\circ]$	$\theta[^\circ]$
$DDES-30l-CFL=1$	19.1	13.0	7.1
$DDES-30l-CFL=3$	18.9	11.9	7.5
Jermann [23]	19	12	5.5
Lehugeur et al. [29]	18	-	7
Thacker [49]	18.8	14.7	6.2

5.2.3 Grid refinement over the slanted surface

Here, the influence of the refinement of the grid over the slanted surface is studied on the $30l$ grid with $CFL=3$. Drag and lift coefficients, and the recirculation bubble length are compared to experiments for different L_{ref} values and are detailed in Tab. 6. The Ref annotation in tables for $30l-L_{ref}=3mm$ corresponds to the reference grid detailed in Sect. 4. The flow is massively separated for $L_{ref}=10mm$. The massive separation is linked to the prism/tetrahedron cells transitions over the slanted surface. Indeed, high value of L_{ref} leads to a strong transition in the different cells size, which may locally increase the numerical dissipation, then compromising the good resolution of the flow. Below this limit, there is no improvement of the flow.

This comparison on the grid refinement over the slant surface shows that, even though LES grid cell size is recommended for the LES part of the DDES model [47], there is no need to refine the mesh too much in the separation area. In reality, the good representation of the boundary layer through the prism layers is more important, as all scales onset in the near wall area. Moreover, for mesh with tetrahedron cells, the authors recommend the use of $L_{ref}=5mm$ in recirculation area. It allows a fair reproduction of the real flow and saves some computational time compared to $L_{ref}=3mm$ (around 2 million cells for the Ahmed body, which can lead to a significant reduction for a real car, which is in average four or five time bigger than the Ahmed body).

Table 6 Comparisons of drag and lift coefficients and recirculation bubble length between experiments and DDES for different L_{ref} values for the $30l$ grid

Configurations	Total cells number [Million]	C_d	$\Delta C_d[\%]$	C_l	$\Delta C_l[\%]$	$L_R[\%]$
Exp. [41]	-	0.356	± 0.5	0.311	± 1	78
$30l-L_{ref}=3mm=REF$	22	0.347	- 2.5	0.323	3.9	75
$30l-L_{ref}=5mm$	20	0.346	- 2.9	0.325	4.3	77
$30l-L_{ref}=10mm$	18.3	0.268	- 24.5	0.042	-86.5	-

The unsteady behavior of the flow is now studied based on the previous results, using SST DDES model, 30 prism layers near the wall, a Courant number equal to 3 and $L_{ref}=5mm$ over the slanted surface.

5.2.4 Unsteady flow behavior

This part focuses on the unsteadiness behavior of the flow around a 25° Ahmed body.

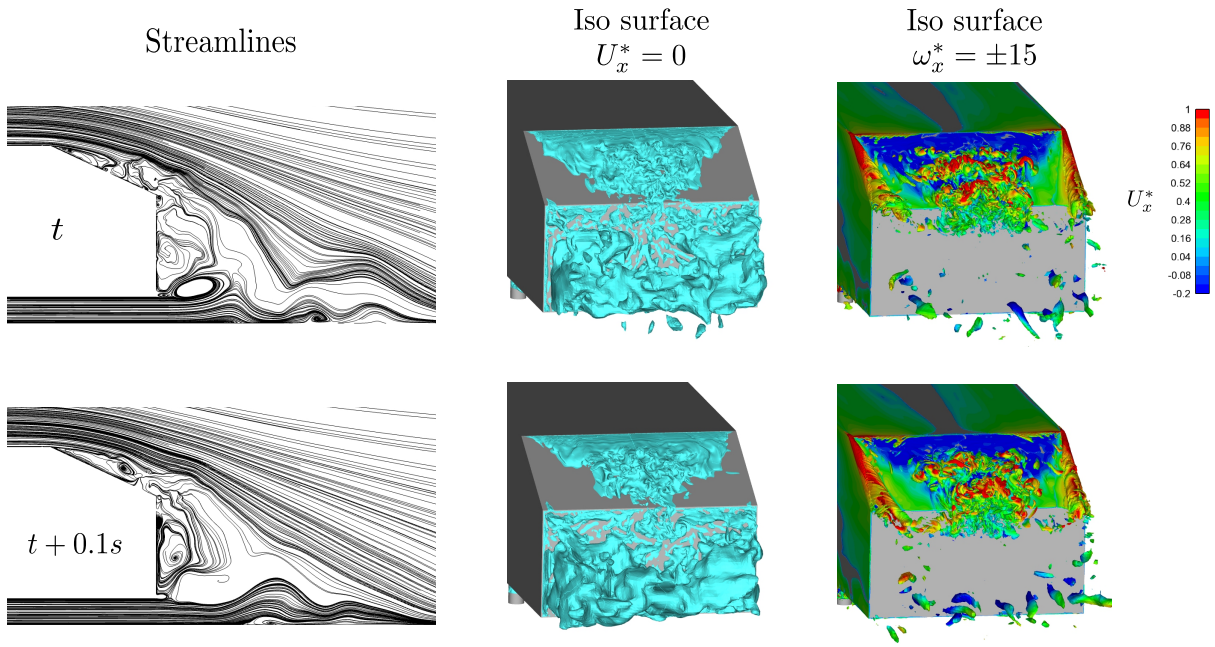

Fig. 21 Unsteady evolution between time t and $t + 0.05s$ of the streamlines, the iso surface of $U_x^* = 0$ and iso surface of $\omega_x^* = \pm 15$

- Unsteady flow snapshot

Fig. 21 displays the unsteady flow behavior from physical time t to $t + 0.05s$ (during averaging process). Streamlines in the symmetry plane, iso surfaces of $U_x^* = 0$ and $\omega_x^* = \pm 15$ are plotted. The streamlines and the iso surface of the velocity indicate the high unsteadiness of the flow on the rear slant surface. Many structures such as hairpin vortices are depicted at this location corresponding to a vortex shedding. Moreover, when a movie is realized from all the gathered snapshots, we can clearly show that the recirculation on the backlight is oscillating in the streamwise direction, describing a flapping motion as detailed in [24]. In fact, the length of the recirculation bubble is alternatively shorter and longer compared to the average length. The same unsteadiness is observed behind the vertical base. The upper and lower recirculation areas are still recognizable, even if the structure look very deformed compared to average plot. The flapping motion is also present in the wake of the body. These motions are studied in the spectral analysis below. Besides, the vorticity plot clearly demonstrates the high stability and strength of the C-pillar vortices over time. The streamwise velocity on the iso surfaces show that the C-pillar vortices are a jet type with freestream velocity in the core [29]. It explains why these vortices are so stable in space and time. These results are in agreement with Krajnović and Davidson work [27]. All of the averaged flow features highlighted in Sect. 2.1 are clearly observable in unsteady snapshots of the flow presented in this section.

- Spectral analysis

As summarized in the introduction, many works have been published on the Ahmed body case but fewer works were conducted on the spectral analysis of the flow around this body, see for example [44, 52, 26, 35] and [10, 49, 24], and rare spectral results were obtained from numerical simulations [10, 26, 35]. Therefore, it is important to keep on simulating this flow with advanced turbulence models in order to give a better understanding of its complex unsteady structures. The numerical and experimental work cited above have shown a series of dominant spectral fluctuations,

each characterized by a Strouhal number (St) which is a dimensionless frequency (based on the height model and the freestream velocity) used to identify unsteady flow dynamics.

Indeed, in [44], the unsteady wake of the Ahmed body with a backlight angle of 25° has been investigated experimentally by Sims-Williams. This study has revealed the presence of a large separation bubble over the entire centerline that corresponds to the von Kármán-like vortex shedding observed at a frequency $St = 0.5$.

A similar value ($St = 0.53$) was found experimentally by Thacker [49], behind the slant, along the back of the 25° Ahmed body. Thacker have also performed spectral analysis of different output signals above the rear slanted surface of the bluff body by using hot wire anemometry, PIV and pressure transducers. Their work has shown both the presence of a high frequency unsteadiness ($St = 0.63$) and low frequencies activity ($St = 0.11$) above the rear slanted surface. The existence of low frequencies seems to be related to a flapping motion. The authors have also detected that the characteristic frequencies depend very little on the Reynolds number.

These observations have been extended by some numerical studies. Krajnovic *et al.* [26] have suggested the presence of two dominating frequencies that correspond to Strouhal numbers $St = 0.15$ and $St = 0.26$. The analysis was based on the Fourier transform of the drag coefficient signal and the pressure coefficient integrated over the rear slanted surface.

In [35], SVV-LES simulations of the flow over the 25° Ahmed body have been performed at $Re_H = 7.6 \times 10^5$. A particular attention has been given to the Fourier analysis of the time variations of the streamwise velocity at different points. Near the separation zone, in the middle of the slant, Minguez *et al.* have found a multifrequency regime with a dominant Strouhal number of $St = 0.27$ which is due to the development of horseshoe vortices. Behind the slant, a higher frequency activity appeared at $St = 0.42$ along the back of the body.

Fig. 22 2D streamlines computed from the mean velocity field of the flow in the plane $z = 0$ and measurement points (from point 1 to point 8) selected for the spectral analysis.

In this work, the unsteady effects developed in the flow along the rear slanted surface and in the near wake of the body are characterized with spectral analysis of velocity and pressure fluctuations. Two techniques are employed : a in-house program which computes the frequency spectrum of a signal by decomposing it in harmonics and the second method is based on the available 'pwelch' function on MATLAB which estimates the power spectral density (PSD) of an input signal with Welch's overlapped segment averaging estimator. These methods are applied with different signals (streamwise velocity component U_x and pressure coefficient C_p) that result from the SST DDES simulation.

In this spectral analysis, different locations of the flow are considered. They are situated along the slanted surface of the Ahmed body and in the back of the body. Fig. 22 represents the 2D streamlines computed from the mean velocity field in the plane $Y^* = 0$ and shows the location of the measurement points whose coordinates are detailed in the first column of Tab. 7. Moreover, Fig. 23 shows, in function of the Strouhal number, the frequency spectrum of the streamwise velocity fluctuations (a) and the Welch PSD estimation of the streamwise velocity fluctuations (b) corresponding to measurement point 1. In Fig. 23 (a), harmonics of the spectrum are of many amplitudes that usually become smaller as they increase in frequency. A dominant Strouhal number represented by 'a peak' appears in the two figures. It equals to 0.48 in the first graph and approximately 0.45 in the second one.

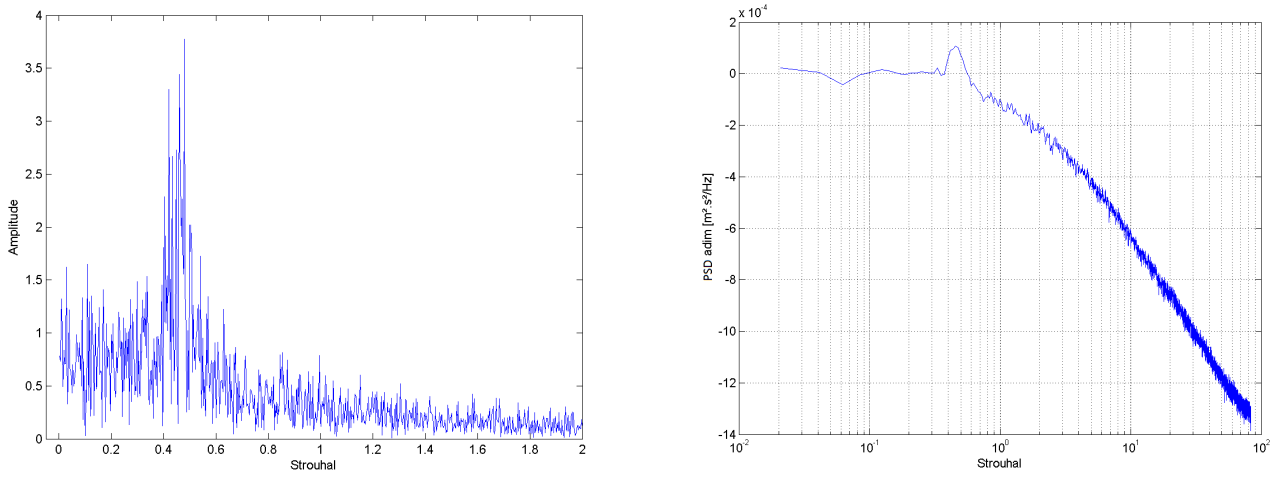

(a) frequency spectrum (b) PSD

Fig. 23 Measurement point 1 : (a) Frequency spectrum of the streamwise velocity fluctuations and (b) PSD adimensionned by the frequency resolution and velocity variance of fluctuations.

To be concise, the dominant Strouhal numbers corresponding to the higher values of this factor are summarized in Tab. 7. They are computed from both frequency spectrum and PSD of the U_x and C_p signals and they are respectively called St_{Ux} and St_p. The dominant frequencies of the vertical velocity component U_z have also been computed for each measurement point and they are of similar magnitude as those calculated with the streamwise velocity component U_x. In the table, the nomination 'MF' means that multiple frequencies appear in the spectrum and the values in parentheses refer to the higher peaks of similar magnitude that still appear. The frequency spectra of the pressure coefficients shows multifrequency regimes for several measurement points.

The dominant Strouhal numbers are in quite good agreement with the frequencies found by Thacker [49] and Minguez *et al.* [35] by considering the measurement points $1,2,3,4,5,6$ whose coordinates are the nearest of those of the points they have selected in their studies. Although the frequencies computed in the recirculation zone along the rear slant ($St = 0.12 - 0.25$) are overestimated comparing with the value $St = 0.11$ found in [49], the fluctuations also belong to the range of low frequencies. Indeed, it results from this study a series of high and low frequency ranges. In the back of the Ahmed body around the recirculation zone, at measurement points 1 and 2, there exist high fluctuations

of order $St = 0.45 - 0.48$ which are closed to the values found by [49] and [35]. This high frequency unsteadiness confirms the presence of the von Kármán-like vortex shedding. In the rear slant, the low frequency flapping of the separated bubble identified at measurement points $3,4,5,6$ is found in a range of frequencies equal to $St = 0.12 - 0.25$ that is slightly lower than the dominant Strouhal number ($St = 0.27$) obtained in [35]. The Strouhal number of the measurement point 3 is a little higher than those of points $4,5,6$ since it is located at the beginning of the recirculation zone where the flow becomes detached from the rear slant surface. In the lateral surfaces (measurement points $7,8$), the longitudinal structures behave like two large counter-rotating conelike trailing vortices (the C-Pillar Vortex) that decelerate the flow. These longitudinal vortices are illustrated in Fig. 2. In this low pressure zone, the flow circulates at multifrequency regime, that may come from the influence of the flow recirculation along the back of the body, however dominant weak peaks emerge around $St = 0.15 - 0.25$.

Points	Coordinates			Flow region	Frequency spectrum		PSD		*St*	*St*
	x	y	z		St_{Ux}	St_p	St_{Ux}	St_p	of Thacker	of Minguez et al.
1	0.129	0	0.052	Wake	0.48	0.48	0.45	0.47	0.53	/
2	0.179	0	0.080	Wake	M (0.23,0.48)	0.48	0.45	0.47	/	0.42
3	-0.196	0	0.335	Rear slant	0.25	0.21	0.25	0.21	0.11	/
4	-0.163	0	0.326	Rear slant	0.21	MF (0.14)	0.21	0.15	0.11	/
5	-0.102	0	0.307	Rear slant	0.20	MF (0.12,0.25)	0.21	0.12	0.11	/
6	-0.070	0	0.286	Rear slant	0.14	MF (0.23,1.6)	0.15	0.14	/	0.27
7	0.040	-0.163	0.263	Longitudinal structures	0.24	MF (0.12,0.23)	MF (0.20,0.45)	0.21	/	/
8	0.120	-0.147	0.244	Longitudinal structures	0.25	0.16	0.12	0.12	/	/

Table 7 Coordinates of measurement points with their flow region and dominant Strouhal numbers computed from the frequency spectra and from the PSD of the streamwise velocity component and the pressure coefficient of the flow respectively called St_{Ux} and St_p.

6 Effects of rounded edges on the flow topology of the Ahmed body

The flow separation on the back (rear window and sides) of the sharp edge Ahmed body generates a closed recirculation bubble and high energetic C-pillar vortices with a high drag contribution. Some simple geometrical modifications as shown experimentally by Rossitto et al. [41] can improve the flow behavior and alter the recirculation bubble and the C-pillar vortices. Rounded edges introduce a passive control strategy with beneficial effects on the drag and lift forces. Three different cases are studied hereafter: the side rounded case R_0S_{10}, the roof rounded case $R_{10}S_0$ and the double rounded case $R_{10}S_{10}$. The three geometries are presented in Fig. 3. The aim of this part is to deepen the study of passive flow control on the Ahmed body using validated hybrid RANS/LES CFD methods and define which rounded location is the best to reduce both drag and lift coefficients.

Based on the work detailed previously, the numerical procedure has been validated on new Ahmed bodies with rounded edges. In this section, the modifications in the flow topology due to the influence of the rounded edges is investigated compared to the reference case with sharp edges. Drag and lift coefficients and flow evolutions are compared on the $20l$ and $30l$ grids, for a CFL number around 3.

Table 8 Comparisons of drag and lift coefficients and recirculation bubble length between experiments and DDES computation on the R_0S_{10} rounded case

Grids	C_d	$\Delta C_d\,[\%]$	C_l	$\Delta C_l\,[\%]$	$L_R\,[\%]\,R_0S_0 \rightarrow R_0S_{10}$	$L_{VB}\,[\%]$
Exp. [41]	0.359	$\pm$0.5	0.241	$\pm$1	78 $\rightarrow$ 85	48
20l	0.347	- 3.3	0.257	6.6	96 $\rightarrow$ 92	46
30l	0.350	- 2.5	0.243	0.8	75 $\rightarrow$ 91	45

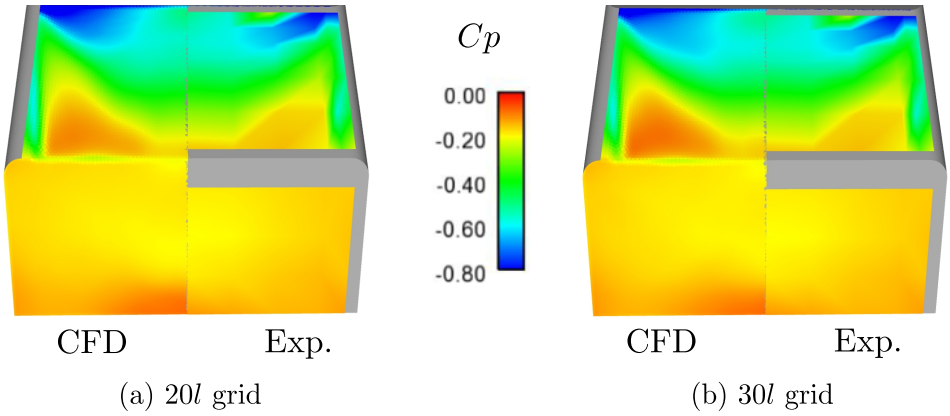

(a) 20l grid (b) 30l grid

Fig. 24 Comparisons of the C_p field on the back of the body with (a) 20l grid and (b) 30l grid, the left part of the picture corresponds to the CFD result and the right part to experiments - R_0S_{10} rounded case

6.1 CFD results on side rounded case - R_0S_{10}

The main flow modification with the side rounded edges concerns the longitudinal vortices. From experiments [41], the onset of the C-pillar vortices is delayed and their intensity reduced. Based on this flow modification, the recirculation bubble over the rear slant surface is longer, from 78% for the reference case to 85%. This results in an increase of 3% for C_d and a decrease of 22% for C_l. Here, we focus on a detailed numerical study of the flow topology analyzing a wide range of results.

6.1.1 Aerodynamic coefficients, recirculation lengths, velocity profiles and C_p

Tab. 8 compares the drag and lift coefficients, the recirculation bubble length L_R over the rear slant surface and L_{VB} behind the vertical base for two different grid levels with 20 and 30 prism layers. Globally, all of these quantities are slightly better computed for the 30l grid over the 20l grid. Moreover, the evolution of L_R is in the right direction for the 30l grid, even if an increase of 16% is obtained compared to 8% in experiments between the reference case and the side rounded case. For the 20l grid, a 4% reduction is observed. This small decrease is opposite to experiments. It confirms the high sensitivity of the flow topology around the Ahmed body.

Fig. 24 represents the C_p evolution along the back of the body. A very accurate prediction is obtained with both grids, confirming the close prediction on drag and lift coefficients, as well as length recirculation over the rear slant surface and behind the vertical base.

Fig. 25 represents the evolution of the mean streamwise velocity in the symmetry planes at four locations: (a) at the end of the roof, (b) and (c) on the rear slant surface and (d) in the wake of the body. At the end of the roof, a

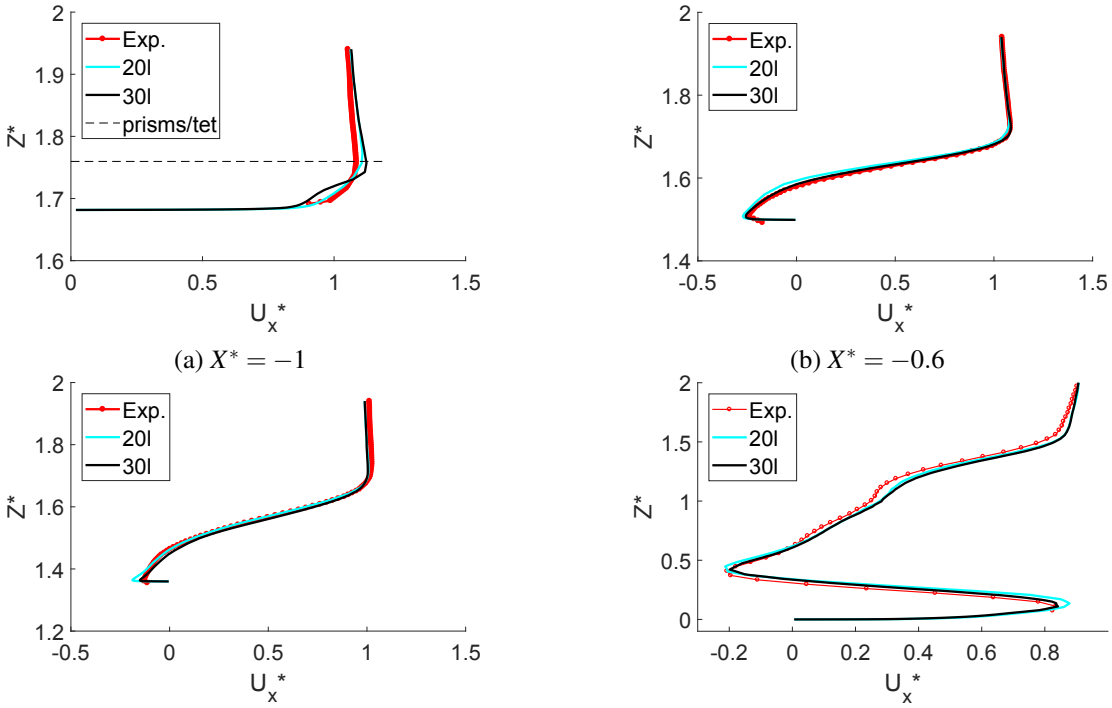

(a) $X^* = -1$ (b) $X^* = -0.6$

(c) $X^* = -0.3$ (d) $X^* = 0.43$

Fig. 25 Profiles of mean streamwise velocity U_x^* for $20l$ and $30l$ grids at the locations $X^* = -1$, $X^* = -0.6$, $X^* = -0.3$ and $X^* = 0.43$ in the symmetry plane of the body $Y^* = 0$ - R_0S_{10} rounded case

slight overestimation for the velocity is observed in computations compared to experiments. It is the same result for the sharp edges case. Moreover, a discontinuity in the profile for the $30l$ grid is coherent with a log layer mismatch ([39], [48]). Indeed, as depicted on the Fig. 26, there is some LES intrusion inside the boundary layer delimited by the transition between the prisms and the tetrahedrons. This intrusion is responsible of the shape of the velocity profile. In the locations on the backlight and the wake, computations profiles are in almost perfect agreement with experiments. These results show the robustness of the numerical procedure for the side rounded edges case.

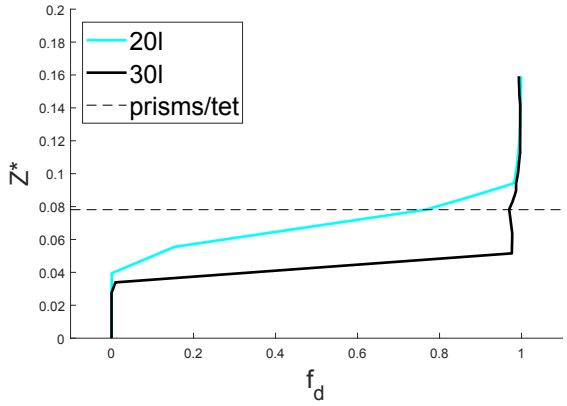

Fig. 26 Evolution of the f_d function for the $20l$ and $30l$ grid at the end of the roof $X^* = -1.1$ - R_0S_{10} rounded case

6.1.2 Physical behavior of the flow

The physical behavior of the flow is studied in Fig. 27 between the R_0S_0 and R_0S_{10} cases using iso surfaces of Q criterion colored by C_p coefficient. The $30l$ grid is used to set the comparison as we do not have any flow visualization of the C-pillar vortices evolution between the two cases from experiments. This figure clearly illustrates the modification of the shape of the C-pillar vortices. The vortices are thinner with the rounded edges and their intensity highly decrease. The level of C_p is increased from -0.8 with the sharp edges to -0.4 with the rounded edges. Moreover, higher C_p value are observed at the onset of the separation at the transition between the roof and the rear slant.

Moreover, the flow topology modification with the side rounded edges is confirmed by the streamlines in the symmetry plane, depicted in Fig. 28. The lower intensity of the C-pillar vortices leads to an increase of the bubble recirculation length over the rear slant surface. As a consequence, due to a larger curvature effects compared to sharp case and the global flow modifications, the recirculations behind the vertical base are shorter. To clarify the figures with streamlines, it may appear that recirculations are not closed, especially behind the vertical base in the saddle point area. It is just a post-processing issue and all of the recirculations on the rear slant surface or in the wake are three-dimensional and closed.

This flow evolution highly influences the drag and lift repartition over the rear part of the body compared to the sharp case, as shown in Tab. 9. C_p values are integrated on the rear slant surface and the vertical base and projected in $(\overrightarrow{x})$ and $(\overrightarrow{z})$ directions to represent respectively drag and lift forces. On the rear slant surface, based on the previous remarks on the flow modification, C_p values are 19.5% higher with the rounded edges, meaning a decrease of 19.5% of drag coefficient (without taking into account the skin friction evolution which is marginal). On the vertical base, due to the shorter recirculation bubble, the C_p values are lower. This results in a 28.3% increase of the drag force. By adding these two contributions, the drag is reduced by around 2% in this part of the flow. Concerning the Cl coefficient evolution, a decrease of 18% is observed. If we can now consider to total drag and lift coefficients around the body, a 1% increase is found on the drag coefficient, very close to the 3% from experiments. The total lift is reduced by 25% compared to the 22% decrease obtained from experiments. Globally, including numerical errors, our results show very good agreement with experiments for both coefficients.

These analysis clearly indicate the flow modifications due to the side rounded edges, leading to a new balancing of the aerodynamic forces around the back of the body. Our numerical results with the SST DDES model are consistent with those of Rossitto et al. [41] from experiments. Despite a sensible change of the flow topology on the rear window (especially regarding the C-pillar vortices strength), the global force balance does not change compared to the sharp case. In fact, as Tab. 9 shows, the C_p contribution from the rear slant surface decrease is canceled by the C_p vertical base increase.

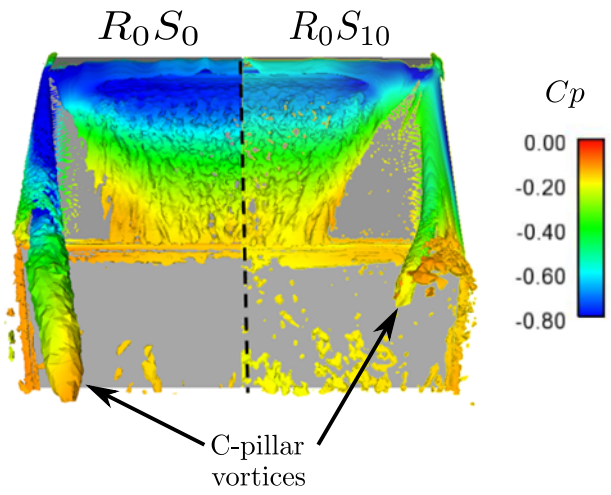

Fig. 27 Comparisons of C-pillar vortices evolution between the reference case R_0S_0 (left) and the side rounded case R_0S_{10} (right) on the $30l$ grid - iso surfaces of $Q = 1.10^5 s^{-1}$

Table 9 Comparisons of C_p integral values on the Rear Slant surface (RS) and on the Vertical Base (VB) along $(\overrightarrow{x})$ and $(\overrightarrow{z})$ axis for the R_0S_0 and R_0S_{10} cases

C_p	R_0S_0	R_0S_{10}	Δ [%]
$RS_{(\overrightarrow{x})}$	-0.230	-0.185	-19.5
$VB_{(\overrightarrow{x})}$	-0.130	-0.167	28.3
$(RS + VB)_{(\overrightarrow{x})}$	-0.360	-0.352	-2.2
$RS_{(\overrightarrow{z})}$	-0.310	-0.254	-18.0

	R_0S_0	R_0S_{10}	Δ [%]
C_d	0.347	0.350	+1
C_l	0.323	0.243	-25

6.2 CFD results on roof rounded case - $R_{10}S_0$

The roof rounded edge increases the velocity of the flow around the rounded corner at the transition roof/backlight. The boundary layer is then more energetic compared to the sharp case and the separation is removed. The original experiments carried out by Rossitto et al. [41] showed that the drag is reduced by 16% and the lift increased by 7%. compared to the sharp case flow. Here again, a detailed numerical study is performed to analyze this flow.

6.2.1 Aerodynamic coefficients, recirculation lengths and C_p

Tab. 10 compares numerical results concerning the drag and lift coefficients, the recirculation bubble length L_R over the rear slant surface and L_{VB} behind the vertical base. A perfect prediction on drag and lift coefficients is obtained for both meshes, with a maximal error of 1.2%. Due to the roof rounded edges, there is no separation on the rear slant surface, as observed in experiments. The recirculation length behind the vertical base is also well predicted with a value of 72% for the two grids compared to 68% in experiments. Fig. 29 represents the C_p evolution along the back of the body. For

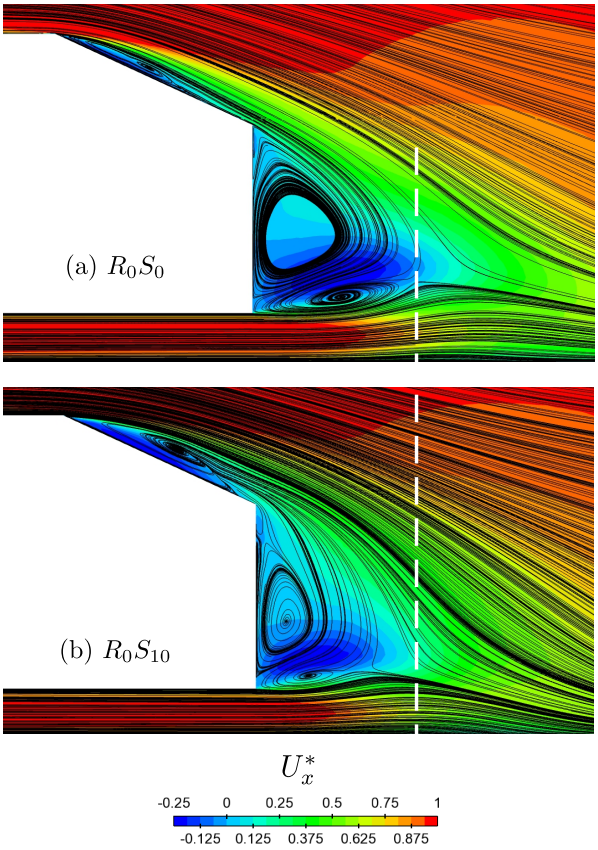

Fig. 28 Comparisons of streamlines colored by the mean streamwise velocity U_x in the symmetry plane $Y^* = 0$ between the reference case R_0S_0 and the side rounded case R_0S_{10} on the $30l$ grid

both grids, the prediction is very accurate compared to experiments, with the correct pressure recovery distribution over the backlight. The C_p level is nearly constant on the vertical base and also well reproduced from computations. The footprint of the longitudinal vortices is obvious on the left part of the picture. However, it is not possible to compare precisely the C-pillar vortices to experiments as not enough probes was used during measurements. Finally, the above C_p field and aerodynamic forces show that the numerical procedure for both grids reproduce accurately the flow around the geometry.

Table 10 Comparisons of drag and lift coefficients and recirculation bubble length between experiments and DDES computation on the $R_{10}S_0$ case

Grids	C_d	$\Delta C_d\,[\%]$	C_l	$\Delta C_l\,[\%]$	$L_R\,[\%]$	$L_{VB}\,[\%]$
Exp. [41]	0.297	± 0.5	0.333	± 1	0	68
$20l$	0.299	0.7	0.337	1.2	0	72
$30l$	0.297	0.0	0.332	-0.3	0	72

6.2.2 Physical behavior of the flow

To better understand the flow modifications with the roof rounded edge, Fig. 30 plots the mean streamwise velocity profiles at the end of the roof in the symmetry plane $Y^* = 0$ with the $30l$ grid. It is quite obvious that by getting close to

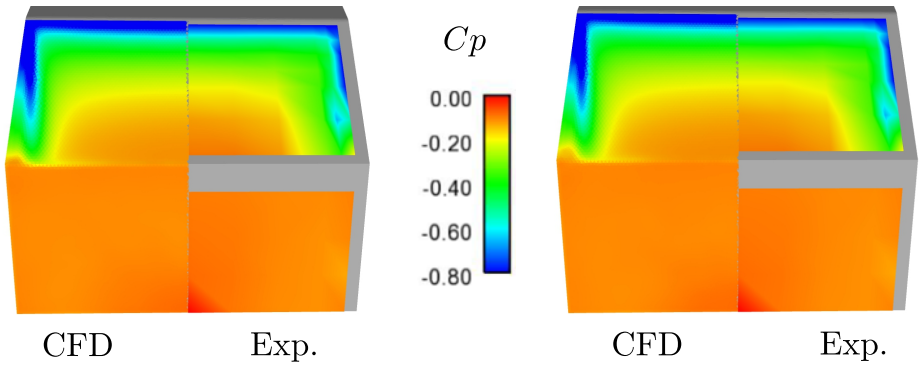

(a) $20l$ grid (b) $30l$ grid

Fig. 29 Comparisons of the C_p field on the back of the body with (a) $20l$ grid and (b) $30l$ grid, the left part of the picture corresponds to the CFD result and the right part to experiments - $R_{10}S_0$ rounded case

the rounded edge, the velocity increases to reach 1.35 compared to 1.2 for the sharp edges case. Moreover, the velocity growth takes place in the inner part of the boundary layer, enforcing its capability to resist to separation. Then, as there is no separation on the rear slant surface, the flow topology in the wake of the body is influenced. Fig. 31 depicts the streamlines colored by the mean streamwise velocity in the symmetry plane of the body. The recirculation length behind the vertical base is increased from 45% to 72%, which is consistent with experiments (from 48% to 68%). The lack of separation leads to a longer recirculation in the wake. Indeed, the separation induces curvature in the flow over the backlight and tend to roll up the wake behind the vertical base. Without separation, the flow separates massively at the transition backlight/vertical base. Moreover, the size of the two 3D recirculation areas are different, again for the same reasons. With the rounded edge, the upper recirculation is longer and it length now equal to the lower one. This result shows that the lower recirculation is highly dependent of the upper one, as there is no geometry modification at the bottom of the Ahmed body. This new equilibrium of the flow around the back of the body directly leads to a 16% decrease of C_d and 7% increase of C_l. Therefore, we can conclude that the upper rounded edge is an efficient drag reduction tool for a 25° simplified vehicle.

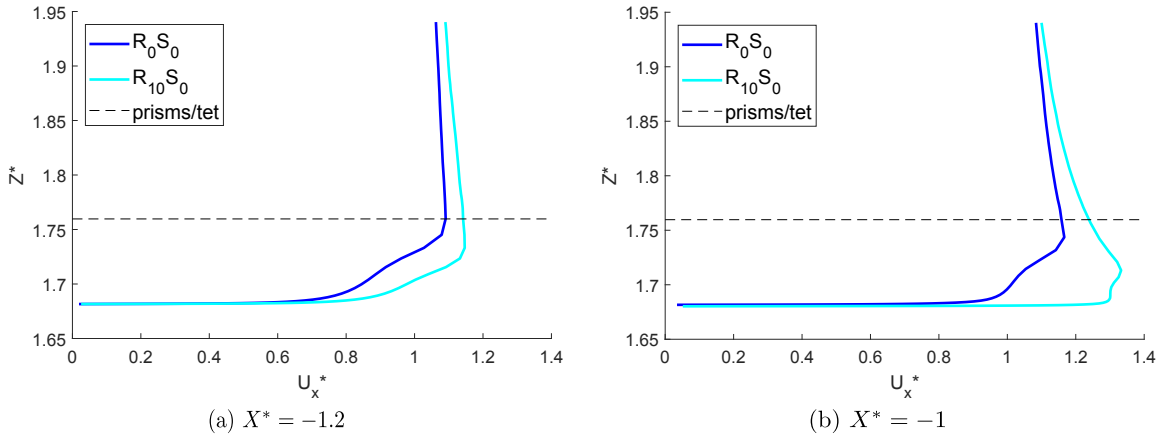

(a) $X^* = -1.2$ (b) $X^* = -1$

Fig. 30 Comparisons of velocity profiles at the end of the roof at the locations (a) $X^* = -1.2$ and (b) $X^* = -1$ between the reference case R_0S_0 and the roof rounded case $R_{10}S_0$ on the $30l$ grid

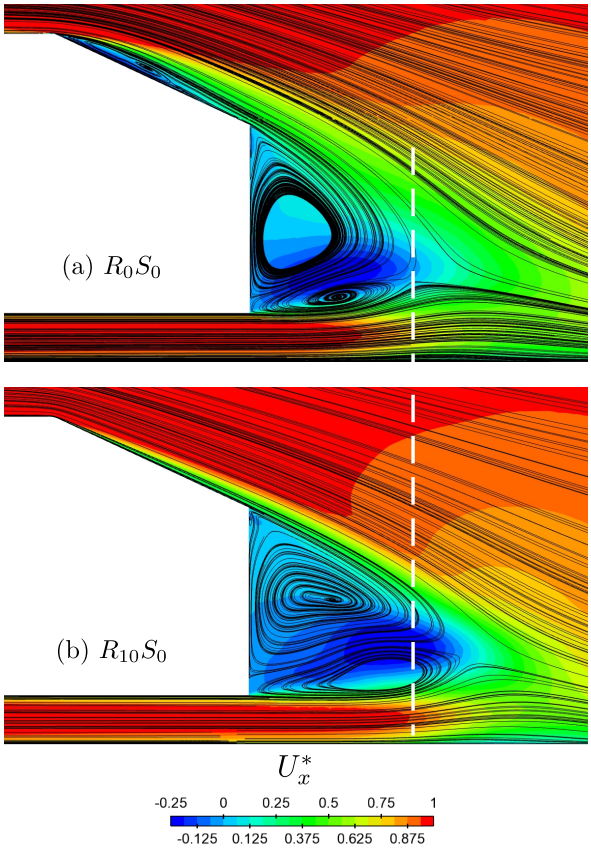

Fig. 31 Comparisons of streamlines colored by the mean streamwise velocity U_x in the symmetry plane $Y^* = 0$ between the reference case R_0S_0 and the roof rounded case $R_{10}S_0$ on the $30l$ grid

6.3 CFD results on double rounded case - $R_{10}S_{10}$

The double rounded case combined the effects of the side and the roof rounded sides. The separation is removed on the rear slant surface and the C-pillar vortices are less energetic. The experiments by Rossitto et al. [41] show a drag decrease of 16% and a lift reduction of 18% compared to the sharp edge body. The main target here is to verify how efficient is such a coupled control compared to simple roof or side rounded edges.

6.3.1 Aerodynamic coefficients, C_p and recirculation lengths

Tab. 11 compares the drag and lift coefficients, the recirculation bubble length L_R over the rear slant surface and L_{VB} behind the vertical base. The $20l$ grid shows very accurate prediction on both C_d and C_l coefficients with an error below 1%. In contrast, the $30l$ grid leads to an overestimation of 7% of C_d. The C_l coefficient is well predicted.

Table 11 Comparisons of drag and lift coefficients and recirculation bubble length between experiments and DDES computation on the $R_{10}S_{10}$ case

Grids	C_d	ΔC_d [%]	C_l	ΔC_l [%]	L_R [%]	L_{VB} [%]
Exp. [41]	0.298	$\pm$0.5	0.254	$\pm$1	0	64
$20l$	0.296	-0.7	0.255	0.4	0	62
$30l$	0.320	7.4	0.253	-0.4	66	55

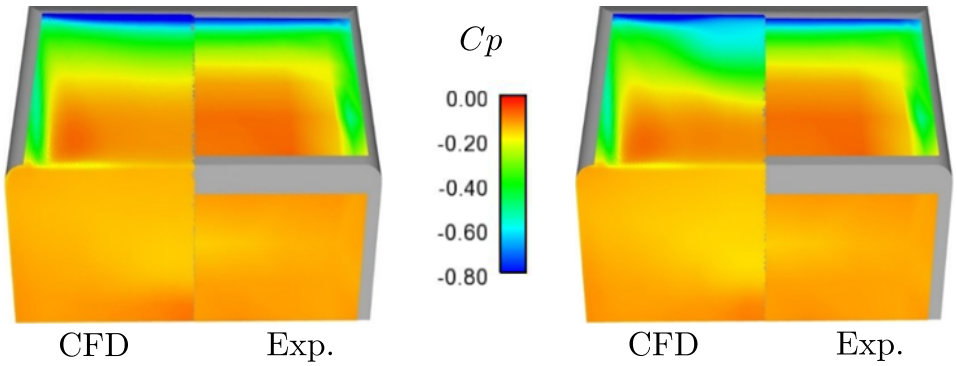

(a) $20l$ grid (b) $30l$ grid

Fig. 32 Comparisons of the C_p field on the back of the body with (a) $20l$ grid and (b) $30l$ grid, the left part of the picture corresponds to the CFD result and the right part to experiments - $R_{10}S_{10}$ rounded case

The drag overestimation with the $30l$ grid can be explained when looking at the C_p field on the back of the body in Fig. 32. The left part of the figure corresponds to CFD results and the right part to experiments. It is clear that a separation occurs on the backlight with the $30l$ grid, with lower C_p at the top compared to experiments. The recirculation length is equal to 66%. For the $20l$ grid, no separation is observed and the C_p prediction is very close to experiments. It is interesting to notify that for the side rounded and roof rounded cases, the $30l$ grid presents very accurate prediction on drag and lift coefficients and flow topology. However, with the combination of the rounded areas on the body, a non physical separation appears with this grid and is analyzed in the next section.

6.3.2 Increasing the shielding of the DDES model

These results show all of the complexity of the use of the DDES model. Instinctively, users want to refine the grid, especially in area such the rounded edges of the geometry, in order to discrete as much as possible the real shape of rounded edges and resolve more flow detail. However, for such case, when the grid is too fine near the wall, it leads to MSD (Modeled Stress Depletion) and GIS (Grid Induced Separation) and the solution is altered (separation non expected in our case). There is two ways to correct such issue: the first one is to coarsen the grid near the wall by taking the risk of loosing crucial information for the flow resolution ; the second one is to increase the shielding of the DDES model. Ashton et al. [5] have shown that in some case the shielding of the DDES model is not strong enough, leading to GIS. To remedy this situation, Ashton [6] has studied the influence of the Cd_1 parameter in the f_d function of the DDES model (Eq.7), with the objective of increasing the shielding of the model. This work was realized on three distinct cases: a flat plate, the 25° Ahmed body and a high-lift three-element airfoil. The default value of the Cd_1 parameter is 20 in the SST DDES model. The author advices a value around 25 to increase the shielding while avoiding to delay too far the transition RANS/LES and the onset of resolved turbulent structures in the flow.

In our case, we have compared the Cd_1 values from 20 (reference value), to 25 and 30. Tab. 12 compares the drag and lift coefficients, the recirculation bubble length L_R and L_{VB} for the $30l$ grid. There is no significant changes between

Table 12 Comparisons of drag and lift coefficients and recirculation bubble length between experiments and DDES computation on the $R_{10}S_{10}$ case

Grids	C_d	$\Delta C_d\,[\%]$	C_l	$\Delta C_l\,[\%]$	$L_R\,[\%]$	$L_{VB}\,[\%]$
Exp. [41]	0.298	± 0.5	0.254	± 1	0	64
$30l - Cd_1 = 20 - REF$	0.320	7.4	0.253	-0.4	66	55
$30l - Cd_1 = 25$	0.317	6.5	0.253	-0.4	70	53
$30l - Cd_1 = 30$	0.298	-0.1	0.249	-1.8	0	64

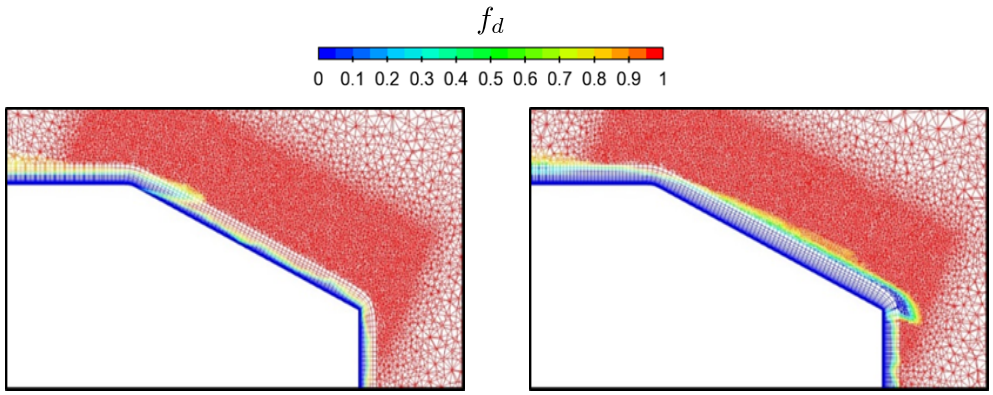

(a) $30l$ grid - $Cd_1 = 20$ (b) $30l$ grid - $Cd_1 = 30$

Fig. 33 Comparisons of the shielding function f_d at the back of the body on the $30l$ grid with (a) $Cd_1 = 20$ and (b) $Cd_1 = 30$ - $R_{10}S_{10}$ rounded case

the computations with Cd_1 equal to 20 and 25. However, for a value of 30, the separation is removed on the backlight. It leads to a very accurate prediction on both drag and lift coefficients, with a maximum error of 1.8%. The recirculation length behind the vertical base is perfectly predicted compared to experiments. The evolution of the f_d function for $Cd_1 = 20$ and $Cd_1 = 30$ is depicted in Fig. 33. When f_d is equal to 0, the model is in RANS mode. When f_d is equal to 1, the model acts in LES mode. As observed on the figures, the shielding of the boundary layer is enforced at the end of the roof for a value of 30. It means that there is no more LES intrusion inside the boundary layer and the MSD phenomenon is removed. As a consequence, the flow stays attached on the rear slant surface as expected.

The same work has been done for the cases R_0S_0, R_0S_{10} and $R_{10}S_0$. Globally, the boundary layer on the roof is better protected from LES intrusion and the results are still very consistent with experiments. As a consequence, a value of 30 is advised for the Cd_1 constant. The operation of DDES model is strengthened and the shielding increased. It allows the user to generate refine grid near the wall without risking to deteriorate the solution of the computation. It is recommended especially to improve the flow separation behavior.

6.3.3 Physical behavior of the flow

The flow evolution between the reference case with sharp edges R_0S_0 and the double rounded case $R_{10}S_{10}$ is illustrated in Fig. 34. The $30l$ grid with $Cd_1 = 30$ is used to perform the comparison. The left figure plots the evolution of the C_p (a) and the right one the C-pillar (b) evolution using iso surfaces of Q criterion. The left part of the figures corre-

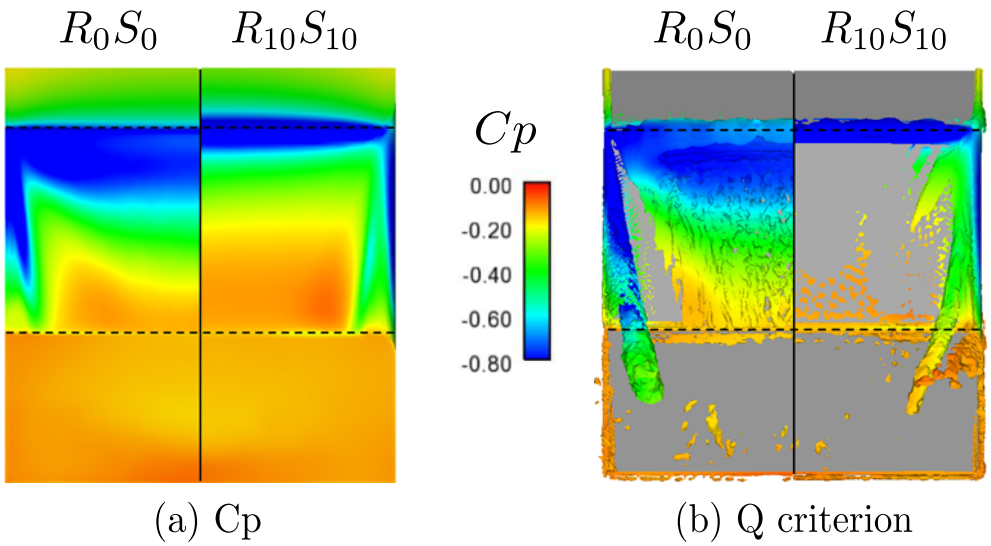

Fig. 34 Comparisons of C_p field (left) and C-pillar vortices (right) evolution between the reference case R_0S_0 and the side rounded case $R_{10}S_{10}$ on the $30l$ grid - iso surfaces of $Q = 1.10^5 s^{-1}$

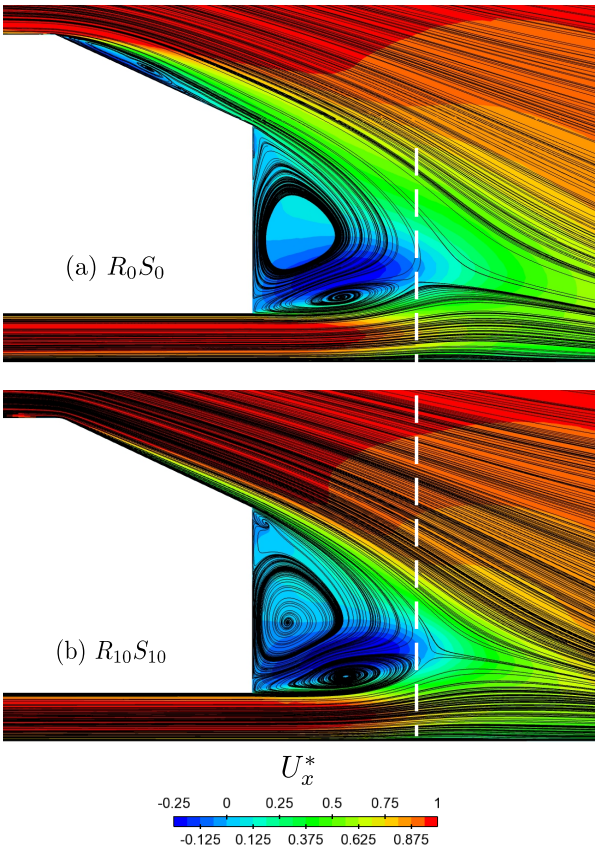

Fig. 35 Comparisons of streamlines colored by the mean streamwise velocity U_x^* in the symmetry plane $Y^* = 0$ between the reference case R_0S_0 and the side rounded case $R_{10}S_{10}$ on the $30l$ grid

sponds to the computation of the R_0S_0 case and the right part to the computation of the $R_{10}S_{10}$ case. Fig. 35 depicts the streamlines colored by the mean streamwise velocity in the symmetry of the body. As early mentioned, the rounded edge at the end of the roof induces a flow acceleration. It leads to very low C_p at the very end of the roof compared to the reference case. Then, as the separation is removed, a pressure recovery is obtained all along the rear slant surface compared to the sharp case which exhibits lower negative C_p values. The vanished recirculation is clearly seen with

the streamlines and also with the iso surfaces of Q criterion, where no turbulent structures are visible on the rear slant surfaces compared to the reference case. On the sides, C_p values are higher as the intensity of the C-pillar is reduced with the rounded edges. In the symmetry plane, the 3D wake with double rounded edges is similar to the sharp case.

All of these flow modifications are responsible for the significant drag and lift reduction accurately reproduced with our computations. These results demonstrate the efficiency of the double rounded edge geometry to design a passive flow control.

The side rounded edge case is designed to improve the drivability skills of the body with a lift reduction. With the roof rounded edge, drag is highly reduced leading to a better efficiency of the model. With both rounded location, drag and lift are reduced in the same way to mix positive effects on the geometry.

7 Discussions on the flow topology around the four Ahmed bodies

To describe the flow topology, the kinematical evolution of the flow can be studied as described in Hunt et al. [20] and applied by Kumar et al. [28]. This method counts the number of separation and attachment points. N and S define respectively node and saddle points and N' and S' respectively half-node and half-saddle points. A well-managed stability study has to respect this formula:

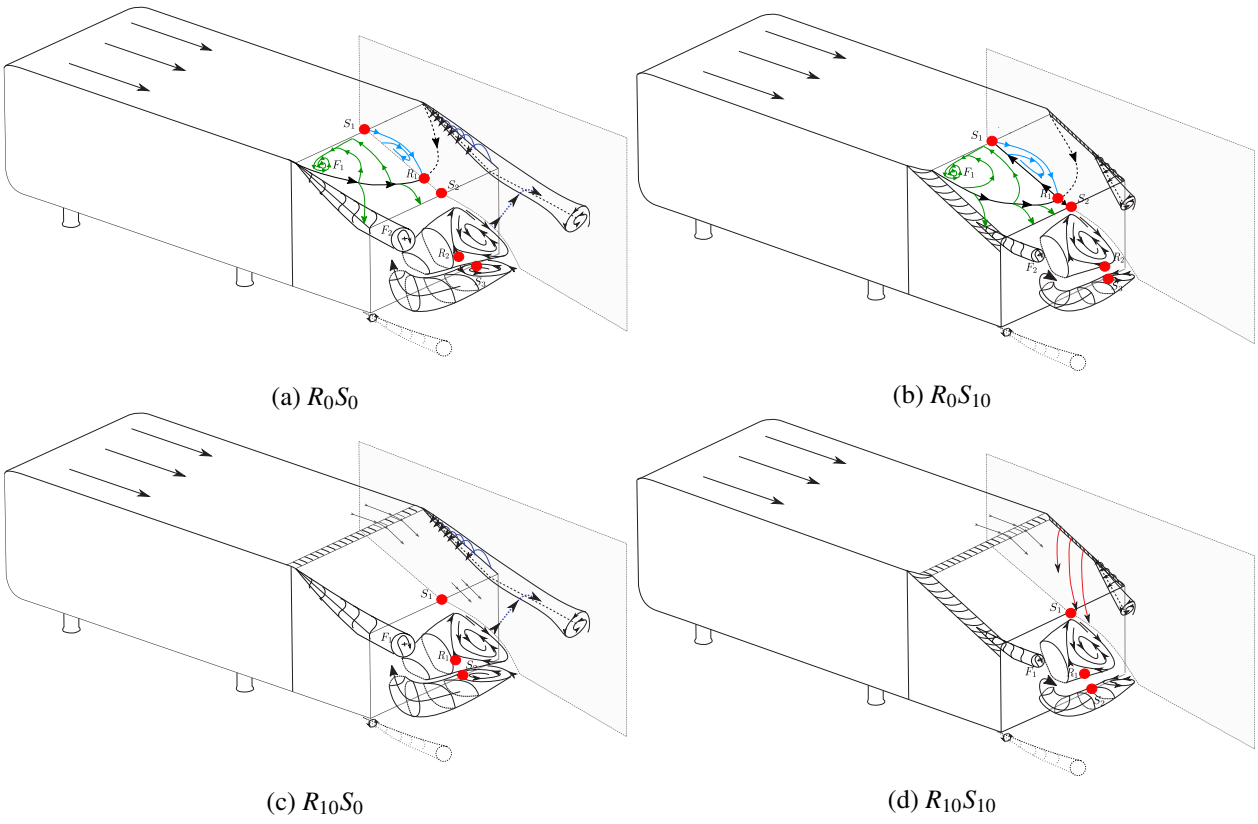

(a) R_0S_0 (b) R_0S_{10}

(c) $R_{10}S_0$ (d) $R_{10}S_{10}$

Fig. 36 Flow topology around the four Ahmed bodies studied

$$(\sum N + \frac{1}{2}\sum N') - (\sum S + \frac{1}{2}\sum S') = 1 - n \tag{14}$$

with n representing the connectivity of the flow section studied. However, using this method is not easy to implement on a turbulent 3D case with high interactions between flow features around the body. For these reasons, Fig. 36 sketches a schematic representation of the flow topology for the four Ahmed studied, with sharp and rounded edges, based on the averaged flow around the bodies. Here, critical points representing separation and reattachment spots as well as recirculation centers are represented for all cases. Separation and reattachment points are shown by red circles around the symmetry plane and denoted by the letters S and R. Recirculation centers are sketched as black crosses and denoted by the letter F giving a better understanding of the critical topological cornerstones. As shown the side rounded edges R_0S_{10} give weaker recirculation spots and the roof rounded edges as well as coupled edge cases $R_{10}S_0$ and $R_{10}S_{10}$ generate fewer and lower central critical points.

From structural point of view, as Fig. 36 (a) shows, the flow pattern depicted for the R_0S_0 case is similar to Jermann [23] and quite different from Ahmed et al. [1] in Fig. 2. The common feature is the closed recirculation bubble on the rear slanted surface generated by the sharp corner at the transition between the roof and the rear slant. The unsteadiness of the recirculation is highlighted in Sect. 5.2.4. Concerning the C-pillar vortices, there are different point of view as we better understand the flow evolution with recent works. Ahmed et al. [1] explained that the C-pillar vortices behave as conic extension vortices all along the wake. Jermann [23] showed that in fact a vortex breakdown of the C-pillar vortices appear around $X^* = 0.89$ as a sudden decrease in vorticity and streamwise velocity is observed.

For the R_0S_{10} case, the onset of the longitudinal vortices are delayed and their intensity highly reduced compared to sharp case. This leads to higher length recirculation over the rear slant surface compared to R_0S_0 case. The separation induces curvature in the flow over the backlight and tends to increase the roll up of the wake, leading to a shorter wake compared to sharp case. Concerning the $R_{10}S_0$ case, the separation bubble over the rear slant surface vanishes due to the rounded edges on the roof. Due to the flow attachment on the backlight, the wake behind the vertical base is longer compared to R_0S_0 and R_0S_{10} cases. Finally, the double rounded edges $R_{10}S_{10}$ case combines the effects of the rounded edges on the roof and on the sides of the Ahmed body.

The rounded edges highly influence the flow topology on the rear slanted surface: suppression of the separation bubble and/or reduction of the C-pillar vortices strength. The wake keeps the same shape even if the recirculation length differs depending on the case. These modifications on the flow structures have a direct influence on local pressure and velocity fields and consequently on drag and lift coefficients as numerically explained through this work.

8 Conclusions

The aim of this work was to use the best SRS procedure to compute the flow around the 25° Ahmed bodies with sharp edge and study a passive control case with rounded edges. First, SST RANS and three hybrid turbulence approaches was studied and compared to in house experiments on this case. The overall best flow prediction is obtained with the

SST DDES model, as SAS suffers from predicting the shape and length of the recirculation bubble and SBES leads to shorter recirculation area on the rear slanted surface. The worse results are obtained with SST RANS model, with a massive separation observed on the back window. Hence, SST DDES model was chosen for the prediction of the flow around the Ahmed bodies. A grid refinement was then performed to establish the numerical convergence. Hybrid meshes were used with prism cells for the resolution of the boundary layer and tetrahedron cells elsewhere in the computational domain. In fact, the use of the SST RANS model in the near wall area restricts the user to set the first node of the grid into the sub-viscous layer of the boundary layer, as $y^+ < 1$ and below 1 if possible. The three grids generated with respectively 15, 20 and 30 prism layers respect this constraint. The most important need is to generate a grid with at least 15/20 nodes in the boundary layer, even though more layers are advised. The best prediction of the flow is obtained with the more refined 30l grid. Increasing the CFL number from values around 1 to 3 (time step three times larger in order to save computational resources) in the separation area also showed that the 30l grid is slightly sensitive to CFL evolution. Drag and lift coefficients presented very good agreement with experiments. The bubble recirculation length is lightly reduced with higher CFL number, from $L_R = 85\%$ to $L_R = 75\%$. In fact, the longitudinal vortices are stronger in intensity leading to a shorter recirculation area over the backlight. The authors advised a more refined mesh (20 or 30 layers grids) with slightly higher CFL values (around 3) with implicit temporal integration scheme. The grid refinement influence over the rear slanted surface for the 30 layers grids has shown that a grid refinement L_{ref} equal to 5 or 7 mm is necessary to achieve an accurate computation. Moreover, a spectral analysis was proposed in order to extract the unsteady structures of the flow in the wake of the body. Thanks to the dominant Strouhal numbers (velocity and pressure signals), the existence of both high and low frequency activities was verified. The highest frequency was found in the back of the body around the recirculation zone and corresponds to the presence of von Kármán-like vortex shedding. In the middle of the rear slanted surface, the frequencies are lower and seem to be related to a flapping motion of the separated bubble.

Based on these results, the Ahmed body configurations with rounded edges were numerically studied and compared again to in house experiments. The first passive flow control device studied was the side rounded case. In this configuration, the onset of the longitudinal vortices are delayed, leading to a longer recirculation bubble on the rear slant surface. Drag is increased by 3% and lift decreased by 22%. DDES results reproduce this flow modification and well predict the drag and lift coefficients evolution. At this location on the Ahmed body, the rounded edges act as a lift reduction tool. The second passive flow control device was the roof rounded case. In this case, the separation on the rear window is suppressed and the wake behind the vertical base is longer. This tow topology change leads to a drag reduction of 16% very well estimated with DDES. The roof rounded edge is an efficient drag reduction tool for this case. The third flow control device use both side and roof rounded edges. Once again, drag and lift coefficients, C_p or velocity fields are accurately predicted using SST DDES for both grids. This setup leads to a decrease of both drag and lift coefficients of 16% and 18%. This work demonstrated the capabilities of the numerical procedure using SST DDES to precisely predict the flow around the 25° Ahmed body with sharp edges. Moreover, the method was able

to accurately take into account the passive control device used on the body with rounded edges at strategic locations of the flow and reproduce significant flow modification. The double rounded configuration shows the best reduction regarding drag and lift forces. This leads to a higher fuel efficiency of the simplified geometry and an improved stability compared to the reference case.

Hybrid RANS/LES model have shown superiority over RANS turbulence model for predicting the flow over the 25° Ahmed body with sharp and rounded edges. The rounded edge shape modification appears as an efficient passive flow control for this geometry.

Nevertheless, a significant effort need to be done to study the flow around real vehicles. A first attempt was done by Heft et al. [19] on the DrivAer model that can be modulated as fastback, notchback and estate shape. The first results in the literature ([4], [16]) shows once more superiority of hybrid methods over RANS models. These studies clearly indicate that no model can well predict the flow topology and aerodynamic coefficients for all geometries. A common strategy should be employed for both notchback and fastback vehicles. Due to massive separation, another approach is needed for the estate shape.

Acknowledgments

The authors would like to thank Prof. Jean-Christophe Robinet (ENSAM Paris, DYNFLUID laboratory) for interesting discussions related to the studied subject.

References

1. Ahmed, S. R., G. Ramm, G. Faltin: Some salient features of the time-averaged ground vehicle wake. *SAE Technical Paper Series* **840300**, Detroit (1984)
2. ANSYS Fluent Theory Guide, Release 17.0 (2016)
3. Ashton, N., A. Revell: Key factors in the use of DDES for the flow around a simplified car. International Journal of Heat and Fluid Flow **54**, 236-249 (2015)
4. Ashton, N., West, A., Lardeau, S., Revell, A.: Assessment of RANS and DES methods for realistic automotive models. Computers Fluids, **128**, 1-15 (2016)
5. Ashton, N., West, A., Mendona, F.: Flow Dynamics Past a 30P30N Three-Element Airfoil Using Improved Delayed Detached-Eddy Simulation. AIAA Journal, 3657-3667 (2016)
6. Ashton, N.: Recalibrating Delayed Detached-Eddy Simulation to eliminate modelled-stress depletion. In 23rd AIAA Computational Fluid Dynamics Conference (2017)
7. Bruneau, C. H., Creusé, E., Depeyras, D., Gilliéron, P., Mortazavi, I.: Coupling active and passive techniques to control the flow past the square back Ahmed body. Computers Fluids, **39(10)**, 1875-1892 (2010)
8. Bruneau, C. H., Creusé, E., Depeyras, D., Gilliéron, P., Mortazavi, I.: Active procedures to control the flow past the Ahmed body with a 25 rear window. International Journal of Aerodynamics, **1(3-4)**, 299-317 (2011)

9. Bruneau, C. H., Creusé, E., Depeyras, D., Gilliéron, P., Mortazavi, I.: Active and passive flow control around simplified ground vehicles, Journal of Applied Fluid Mechanics, **Vol. 5**, No. 1, 89-93 (2012)
10. Ceyrowsky, T., Brcker, Ch., Schwarze, R.: URANS Simulations of the Flow around the AHMED Reference Body, EUROMECH Colloquium **509** 'Vehicle Aerodynamics', Berlin (2009)
11. Choi, H., Lee, J., and Park, H.: Aerodynamics of Heavy Vehicles, Annual Review of Fluid Mechanics **46**, 441-468 (2013)
12. Fröhlich, J., Mellen, C.P., Rodi, W., Temmerman, L., and Leschziner, M.: Highly resolved large-eddy simulation of separated flow in a channel with streamwise periodic constrictions, Journal of Fluids Mechanics **526**, 19-66 (2005)
13. Gritskevich, M. S., Garbaruk, A. V., Schtze, J., Menter, F. R.: Development of DDES and IDDES Formulations for the $k-\omega$ Shear Stress Transport Model. Flow, turbulence and combustion, **88(3)**, 431-449 (2012)
14. Guilmineau, E.: Computational study of flow around a simplified car body. Journal of wind engineering and industrial aerodynamics, **96(6)**, 1207-1217 (2008)
15. Guilmineau, E., Deng, G., Wackers, J.: Numerical simulation with a DES approach for automotive flows. Journal of Fluids and Structures, **27(5)**, 807-816 (2011)
16. Guilmineau, E.: Numerical simulations of flow around a realistic generic car model. SAE International Journal of Passenger Cars-Mechanical Systems, **(2014-01-0607)**, 646-653 (2014).
17. Guilmineau, E., Deng, G. B., Leroyer, A., Queutey, P., Visonneau, M., Wackers, J.: Assessment of hybrid RANS-LES formulations for flow simulation around the Ahmed body. Computers & Fluids (2017)
18. Haase, W., Aupoix, B., Bunge, U., Schwamborn, D. (Eds.).: FLOMANIA-a European initiative on flow physics modelling: results of the European-Union funded project, 2002-2004 Vol. 94 Springer Science & Business Media (2006)
19. Heft, A. I., Indinger, T., Adams, N. A.: Introduction of a new realistic generic car model for aerodynamic investigations (No. 2012-01-0168). SAE Technical Paper (2012)
20. Hunt, J. C. R., Abell, C. J., Peterka, J. A., and Woo, H.: Kinematical studies of the flows around free or surface-mounted obstacles; apllying topology to flow visualization, Journal Fluid Mechanics,**(vol. 86)**, part 1, 179–200 (1978)
21. Jasak, H., Weller, H.G, and Gosman, A.D.: High resolution NVD differencing scheme for arbitrarily unstructured meshes, International Journal for Numerical Methods in Fluids, **31**, 431-449 (1999)
22. Jermann, C., Pujals, G., Meliga, P., Serre, E., and Gallaire, F.: Characterization of the streamwise vortices and near-wake dynamics in the turbulent flow around the 25° Ahmed body based on spiv. In Contrôle des décollements: Separated flow control and aerodynamic performance improvements (2013)
23. Jermann, C.: Eclatement tourbillonnaire dans le sillage turbulent d'un véhicule générique. PhD thesis, Aix-Marseille universit (2015)
24. Joseph, P. Amandolèse, X. Aider, J.-L., Drag reduction on the 25 degrees slant angle Ahmed reference body using pulsed jets. Experiments in Fluids, **52**. 10.1007/s00348-011-1245-5 (2012)
25. Kapadia, S., Roy, S., Vallero, M., Wurtzler, K., Forsythe, J.: Detached-eddy simulation over a reference Ahmed car model. In Direct and Large-Eddy Simulation V. Springer Netherlands, 481-488 (2004)
26. Krajnović, S., Davidson, L.: Flow around a simplified car, part 1: large eddy simulation. Journal of Fluids Engineering, **127(5)**, 907-918 (2005)
27. Krajnović, S., Davidson, L.: Flow around a simplified car, part 2: understanding the flow. Journal of Fluids Engineering, **127(5)**, 919-928 (2005)
28. Kumar, D., Sourav, K., Sen, S., Yadav, P. K.: Steady separation of flow from an inclined square cylinder with sharp and rounded base. Computers Fluids, **171**, 29-40 (2018)
29. Lehugeur, B., Gilliron, P., Ta-Phuoc, L.: Characterization of longitudinal vortices in the wake of a simplified car model. AIAA paper **5383** (2005)
30. Menter, F. R.: Influence of freestream values on k-ω turbulence model predictions. AIAA J, **30(6)**, 1657-1659 (1992)
31. Menter, F. R.: Two-equation eddy-viscosity turbulence models for engineering applications. AIAA journal, **32(8)**, 1598-1605 (1994)

32. Menter, F. R.: A new paradigm in Turbulence Modeling for Aerodynamic Simulations, ANSYS Webinar (2016)
33. Menter, F. R., Kuntz, M.: Adaptation of eddy-viscosity turbulence models to unsteady separated flow behind vehicles. In The aerodynamics of heavy vehicles: trucks, buses, and trains. Springer Berlin Heidelberg, 339-352 (2004)
34. Menter, F. R., Egorov, Y.: The scale-adaptive simulation method for unsteady turbulent flow predictions. Part 1: theory and model description. Flow, Turbulence and Combustion, **85(1)**, 113-138 (2010)
35. Minguez, M., Pasquetti, R., Serre, E.: High-order large-eddy simulation of flow over the Ahmed body car model. Physics of Fluids (1994-present), **20(9)**, 095101 (2008)
36. Minguez, M., Pasquetti, R., Serre, E.: High-order LES of the flow over a simplified car model: On the influence of the Reynolds number. European Journal of Computational Mechanics/Revue Europenne de Mcanique Numrique, **18(7-8)**, 627-646 (2009)
37. Mockett, C.: A Comprehensive Study of Detached-Eddy Simulation. Ph.D. thesis, TUB (2009)
38. Nicoud, F., and Ducros, F.: Subgrid-Scale Stress Modelling Based on the Square of the Velocity Gradient Tensor Flow, Turbulence, and Combustion **62(3)**, 183-200 (1999)
39. Nikitin, N. V., Nicoud, F., Wasistho, B., Squires, K. D., Spalart, P. R.: An approach to wall modeling in large-eddy simulations. Physics of fluids, **12(7)**, 1629-1632 (2000)
40. Rossitto, G.: Influence of afterbody rounding on the aerodynamics of a fastback vehicle, PhD Thesis (2016)
41. Rossitto, G., Sicot, C., Ferrand, V., Bore, J., Harambat, F.: Influence of afterbody rounding on the pressure distribution over a fastback vehicle. Experiments in Fluids, **57(3)**, 1-12 (2016)
42. Rotta, J.C.: Turbulente Strmumgen. BG Teubner Stuttgart (1972)
43. Schwamborn, D., Strelets, M.: ATAAC An EU-project dedicated to hybrid RANS/LES methods. In Progress in Hybrid RANS-LES Modelling, Springer Berlin Heidelberg, 59-75 (2012)
44. Sims-Williams, D.B.: Self-excited aerodynamic unsteadiness associated with passenger cars, Doctoral thesis, Durham University (2001)
45. Smagorinsky, J., General Circulation Experiments with the Primitive Equations. I. The basic Experiment, Monthly Weather Review **91**, 99-164 (1963)
46. Shur, M.L., Spalart, P.R., Strelets, M. and Travin, A.: A Hybrid RANS-LES Approach with Delayed-DES and Wall-Modelled LES Capabilities, International Journal of Heat and Fluid Flow, **29:6**, 1638-1649 (2008)
47. Spalart, P. R., Jou, W. H., Strelets, M., Allmaras, S. R.: Comments on the feasibility of LES for wings, and on a hybrid RANS/LES approach. Advances in DNS/LES, **1**, 4-8 (1997)
48. Spalart, P.R., Deck, S., Shur, M., Squires, K.D., Strelets, M., Travin, A.: A new version of detached-eddy simulation, resistant to ambiguous grid densities, Theor. Comput. Fluid Dyn. **20**, 181-195 (2006)
49. Thacker, A.: Contribution expérimentale l'analyse stationnaire et instationnaire de l'écoulement à l'arrière d'un corps de faible allongement, PhD Thesis (2010)
50. Thacker, A., Aubrun, S., Leroy, A., Devinant, P.: Effects of suppressing the 3D separation on the rear slant on the flow structures around an Ahmed body. Journal of Wind Eng. and Ind. Aerodynamics, **107**, 237-243 (2012)
51. Travin, A., Shur, M., Strelets, M., Spalart, P.R.: Physical and numericals upgrades in the Detached-Eddy Simulation of complex turbulent flows, Fluid Mechanics and its applications 65, 239-254 (2002)
52. Vino, G., Watkins, S., Mousley, P., Watmuff, J. and Mavuri, S.: Flow structures in the near-wake of the Ahmed model:, Journal of Fluids and Structures, **20**, 673-695 (2005)